Summer 8-13-2014

Transverse Thermoelectric Effect

Charles Crawford
cgcrawfo@uno.edu

Recommended Citation

Crawford, Charles, "Transverse Thermoelectric Effect" (2014). *University of New Orleans Theses and Dissertations*. 1866.
https://scholarworks.uno.edu/td/1866

Transverse Thermoelectric Effect

A Thesis

Submitted to the Graduate Faculty of the
University of New Orleans in partial fulfillment of the
requirements for the degree of

Master of Science
in
Applied Physics

by

Charles Crawford

B.S. Louisiana State University in Shreveport, 2010

B.S. Louisiana State University in Shreveport, 2010

August, 2014

Contents

List of Figures

List of Tables

Abstract

Anisotropic thermoelectric effects can be measured in certain materials. Anisotropy can also be simulated using a repeated, layered structure of two materials cut at an angle. Various aspect ratios and angles of inclination are investigated in device geometry in order to maximize the thermopower. Eddy currents have been shown to occur in thermoelectric devices, and evidence of these currents are revealed in finite element analysis of the artificially synthesized anisotropic Peltier effect.

Keywords: thermoelectric effect, Seebeck, Peltier, thermal conductivity, electrical conductivity, heat flux, electric potential, electric field

Chapter 1

Introduction

Thermoelectric effects were first discovered by Thomas Johann Seebeck around 1820. The effect that Seebeck discovered bears his name and occurs when a temperature difference along a block of material causes a potential difference across the block. In 1834 the physicist Jean-Charles-Athanase Peltier found that running an electric current through a junction of two different materials either cooled or heated the junction depending on the direction of current into the junction [1]. This phenomenon is similarly called the Peltier effect after its discoverer. About 20 years after Peltier's contributions, William Thomson (Lord Kelvin) derived a thermodynamic relation between the Seebeck coefficient (S) and Peltier coefficient (Π), i.e. $\Pi = S * T$, where T is the lattice absolute temperature [2].

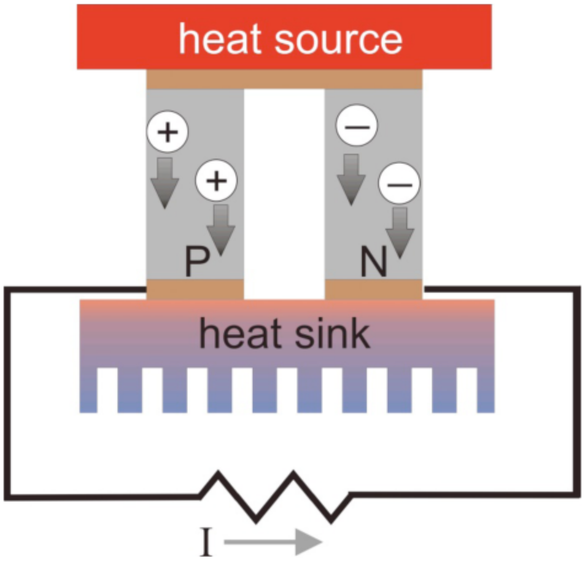

Figure 1.1: Schematic of a thermoelectric couple consisting of an n- and p-type semiconductor operating in power generation mode. A source of heat at the top drives charge carries to the cooler side, producing a current.

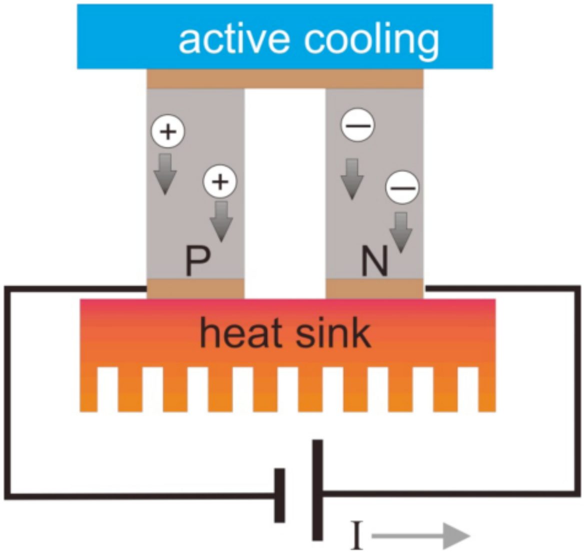

Figure 1.2: Schematic of a thermoelectric couple consisting of an n- and p-type semiconductor operating in cooling mode. A source of current carries heat to the bottom heat sink, cooling the top plate.

Thermoelectric modules are traditionally made using pairs of n-type (electron conducting) and p-type (hole conducting) semiconductors. One couple (called a unicouple) is shown schematically in Fig. 1.1 and Fig. 1.2. Figures 1.1 and 1.2 demonstrate that the thermoelectric can be used for both power generation and solid-state cooling. In a device, many such pairs are connected electrically in series and thermally in parallel, as shown in Fig.1.3 [3].

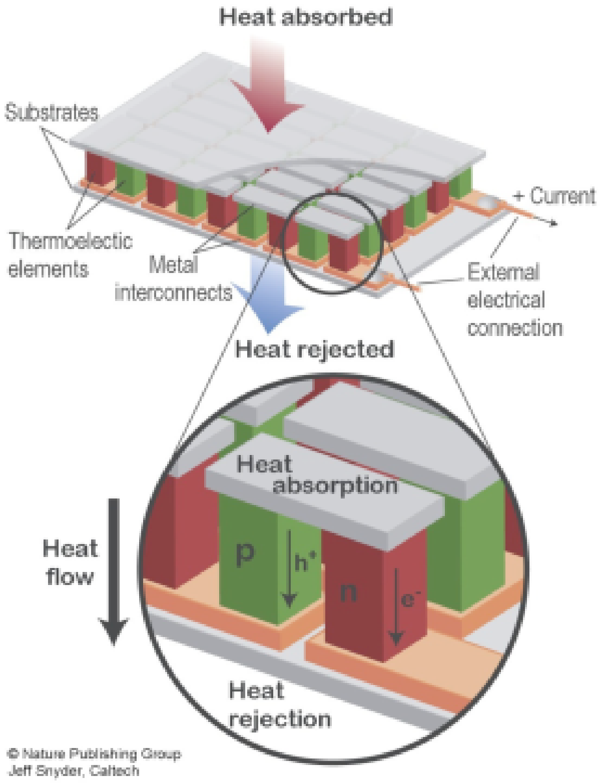

Figure 1.3: Schematic of a longitudinal thermoelectric device in power generation mode.

Thermoelectric research continued into the 20th century and was met with ”excitement and disappointment” [2]. It was thought that thermoelectrics were the next step in power generation, but those hopes dwindled as thermoelectric efficiency never reached the efficiency of traditional generators. This solid state power generation has had some success since the 1940s and 1950s, however, funding has all but disappeared, relatively speaking. The famous Voyager spacecrafts have used longitudinal thermoelectrics since 1977 to power their systems, and the power is expected to last until 2025. The loss of this power source will not only be attributed to the breakdown of the thermoelectric materials which is minimal, but mainly due to the radioactive decay of the plutonium heat source [4]. Other uses include everyday applications such as seat heater/coolers, small refrigerators, and camping equipment for charging phones or GPS location devices.

The transverse thermoelectric effect has the advantage of using only one type of doped semiconductor instead of the two as the longitudinal effect uses. Also, the heat flow and electric current flow in perpendicular direction and, hence, are decoupled. Figures 1.4 and 1.5 illustrate the general geometry of both the transverse thermoelectric effects, Seebeck power generation and Peltier cooling.

Transverse thermoelectric theory has sparked a resurgence in thermoelectric research in recent years. The transverse effect has the potential to reduce the amount of material, relative to longitudinal thermoelectrics, needed for equivalent output power. Since the current cost of sending a pound of anything into space is $10,000, less material for equal output will have a huge effect on the cost of spacecrafts. An important application is the conversion of waste heat to electricity to be put back into the grid. With the modernization of developing countries and ever increasing energy needs of developed countries, the exigency for energy recycling and new methods of creation is paramount.

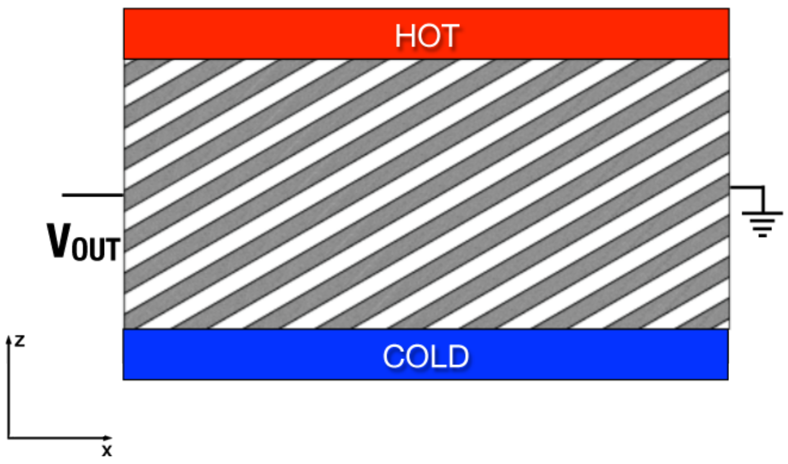

Figure 1.4: Diagram of the transverse Seebeck effect simulation where a temperature difference is in z-direction, and the potential difference is calculated in the x-direction.

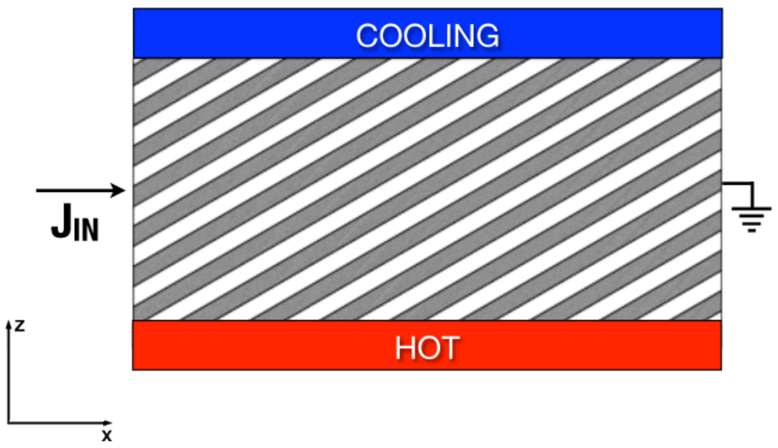

Figure 1.5: Diagram of the transverse Peltier effect simulation where a current is injected in the z-direction, and heat flows in z-direction to cool off the top plate.

Chapter 2

Background

2.1 Transport Equations

2.1.1 Low Field Boltzmann Transport Equation Solution

For thermoelectrics we are interested in the electrical conductivity, thermal conductivity, and Seebeck coefficient. These parameters are dependent on the band structure of the solid, carrier scattering mechanisms, and carrier concentration through the Fermi energy. These physical properties are calculated by first calculating the distribution of electrons as a function of energy using the Boltzmann Transport Equation (BTE). The BTE contains both the gradient of the electrochemical potential (electric field) and the gradient of temperature. Both the electric field and temperature gradient are responsible for the motion of the charge carriers.

This derivation follows closely with Lundstrom's text [5]. Starting with the Boltzmann equation

$$\frac{\partial f}{\partial t} + v \cdot \nabla_r f + \mathbf{F} \cdot \nabla_p f = \frac{\partial f}{\partial t}\Big|_{coll} + s(\mathbf{r}, \mathbf{p}, t) \tag{2.1}$$

$$f_0 = \frac{1}{1 + e^{[E_C(\mathbf{r},\mathbf{p}) - E_F]/k_B T}} \tag{2.2}$$

The relaxation time approximation is used with no source of carriers being injected into the system. So, $s(\mathbf{r}, \mathbf{p}, t) = 0$ and $\frac{\partial f}{\partial t}\Big|_{coll} = -\frac{f_A}{\tau_f}$, and f_A is the function that is being solved for. Since f_0 is symmetric in momentum, the average velocity is zero. Allowing a distribution such that a little current is flowing by thinking of the Fermi distribution as a sum of two parts symmetric f_S and anti-symmetric f_A, gives

$$f = f_S + f_A \tag{2.3}$$

$$f_S = \frac{1}{1 + e^{\Theta}} \qquad where\ \Theta = [E_{C0}(\mathbf{r}, t) + E(\mathbf{p}) - F_n(\mathbf{r}, t)]/k_B T(\mathbf{r}, t) \tag{2.4}$$

$$-\frac{f_A}{\tau_f} = v \cdot \nabla_r (f_S + f_A) + \mathbf{F} \cdot \nabla_p (f_S + f_A). \tag{2.5}$$

With the assumptions

$$f_S \gg f_A,\ |\nabla_r f_S| \gg |\nabla_r f_A|, hspace1mm |\nabla_p f_S| \gg |\nabla_p f_A|$$

the equation simplifies to

$$-\frac{f_A}{\tau_f} = v \cdot \nabla_r f_S + \mathbf{F} \cdot \nabla_p f_S. \tag{2.6}$$

$f_S \equiv f_S(\Theta)$, so the product rule dictates that

$$\nabla_r f_S = \frac{\partial f_S}{\partial \Theta} \nabla_r \Theta \tag{2.7}$$

and

$$\nabla_p f_S = \frac{\partial f_S}{\partial \Theta} \nabla_p \Theta. \tag{2.8}$$

Using Eq. 2.6 and working out the derivatives $\nabla_r \Theta$ and $\nabla_p \Theta$

$$-\frac{f_A}{\tau_f} = v \cdot \frac{\partial f_S}{\partial \Theta} \nabla_r \Theta + \mathbf{F} \cdot \frac{\partial f_S}{\partial \Theta} \nabla_p \Theta \tag{2.9}$$

$$\nabla_p \Theta = \frac{\partial E(\mathbf{p})}{\partial p} \left(\frac{1}{k_B T} \right) = \frac{v}{k_B T} \tag{2.10}$$

$$\nabla_r \Theta = \frac{[\nabla_r E_{C0}(\mathbf{r}) - \nabla_r F_n(\mathbf{r})]}{k_B T(\mathbf{r})} + [E_{C0}(\mathbf{r}) + E(\mathbf{p}) - F_n(\mathbf{r})] \nabla_r \left(\frac{1}{k_B T(\mathbf{r})} \right) \tag{2.11}$$

$$-\frac{f_A}{\tau_f} = \frac{\partial f_S}{\partial \Theta} \left(v \cdot \nabla_r \Theta - \nabla_r E_{C0} \cdot \nabla_p \Theta \right) \qquad where \;\; -\nabla_r E_{C0}(\mathbf{r}) = \mathbf{F} \tag{2.12}$$

$$-\frac{f_A}{\tau_f} = \frac{\partial f_S}{\partial \Theta} \left(v \cdot \nabla_r \Theta - v \cdot \frac{\nabla_r E_{C0}}{k_B T} \right) \tag{2.13}$$

$$-\frac{f_A}{\tau_f} = \frac{\partial f_S}{\partial \Theta} v \cdot \left(\frac{[-\nabla_r F_n(\mathbf{r})]}{k_B T(\mathbf{r})} + [E_{C0}(\mathbf{r}) + E(\mathbf{p}) - F_n(\mathbf{r})] \nabla_r \left(\frac{1}{k_B T(\mathbf{r})} \right) \right) \tag{2.14}$$

Finally,

$$f_A = \frac{\tau_f}{k_B T}\left(-\frac{\partial f_S}{\partial \Theta}\right) v \cdot \mathcal{F} \tag{2.15}$$

where

$$\mathcal{F} = -\nabla_r F_n(\mathbf{r}) + T[E_{C0}(\mathbf{r}) + E(\mathbf{p}) - F_n(\mathbf{r})]\nabla_r\left(\frac{1}{T}\right) \tag{2.16}$$

$\mathcal{F}$ in Eq. 2.16 is ”interpreted as a generalized force” and does apply when magnetic fields are present since $\mathbf{F} \neq -\nabla_r E_{C0}(\mathbf{r})$ in a magnetic field [5]. The components are now gathered and can start being put together to build the coupled current equations which describe how thermoelectric materials transport electrical and heat flows.

2.1.2 Coupled Current Equations

The equations for electric and heat current densities are, respectively [5],

$$\mathbf{J} = \frac{-q}{\Omega}\sum_{p} v f_A(\mathbf{p}) \tag{2.17}$$

$$\mathbf{J}_Q = \frac{1}{\Omega}\sum_{p} E(\mathbf{p}) v f_A(\mathbf{p}) \tag{2.18}$$

Equation 2.17 says that the electric current is the charge times the average velocity of the moving charges. Equation 2.18 says that the heat flow is the energy times the average velocity of the heat carriers. Lundstrom mentions an important point concerning the velocity in Eq. 2.18. He states that the kinetic energy $E(\mathbf{p})$ should be the energy associated with the random motions of temperature and not the drift energy associated with the average motion of particles in an applied field [5].

Singling out the electric current equation and plugging in our low field solution to the Boltzmann transport equation, we have

$$\mathbf{J} = \frac{-q}{\Omega}\sum_{p} v f_A(\mathbf{p}) \tag{2.19}$$

$$\mathbf{J} = \frac{-q}{\Omega}\sum_{p} v \frac{\tau_f}{k_B T}\left(-\frac{\partial f_S}{\partial \Theta}\right) v \cdot \mathcal{F} \tag{2.20}$$

$$\mathbf{J} = \frac{-q}{\Omega k_B T}\sum_{p} v (v \cdot \mathcal{F}) \tau_f \left(-\frac{\partial f_S}{\partial \Theta}\right) \tag{2.21}$$

Displaying equations in indicial notation will be more revealing. This way the components are seen and evaluated more easily. Using indicial notation the current equation becomes

$$J_i = \frac{-q}{\Omega k_B T} \sum_p v_i v_j \mathcal{F}_j \tau_f \left(-\frac{\partial f_S}{\partial \Theta} \right) \tag{2.22}$$

$$J_i = \frac{-q}{\Omega k_B T} \sum_p v_i v_j \left[\partial_j(-F_n) + T[E_{C0}(\mathbf{r}) + E(\mathbf{p}) - F_n] \partial_j \left(\frac{1}{T} \right) \right] \tau_f \left(-\frac{\partial f_S}{\partial \Theta} \right) \tag{2.23}$$

$$J_i = \sigma_{ij} \partial_i (F_n/q) + B_{ij} \partial_i (1/T) \tag{2.24}$$

where

$$\sigma_{ij} = \frac{q^2}{\Omega k_B T} \sum_p v_i v_j \tau_f(\mathbf{p}) \left(-\frac{\partial f_S}{\partial \Theta} \right) \tag{2.25}$$

$$B_{ij} = \frac{-q}{\Omega k_B T} \sum_p v_i v_j \tau_f(\mathbf{p}) T [E_{C0}(\mathbf{r}) + E(\mathbf{p}) - F_n] \left(-\frac{\partial f_S}{\partial \Theta} \right) \tag{2.26}$$

Now, looking at the heat current equation, we have

$$\mathbf{J}_Q = \frac{1}{\Omega} \sum_p E(\mathbf{p}) v f_A(\mathbf{p}) \tag{2.27}$$

$$\mathbf{J}_Q = \frac{1}{\Omega} \sum_p [E_{C0}(\mathbf{r}) + E(\mathbf{p}) - F_n(\mathbf{r})] \; v \frac{\tau_f}{k_B T} \left(-\frac{\partial f_S}{\partial \Theta} \right) v \cdot \mathcal{F} \tag{2.28}$$

$$\mathbf{J}_Q = \frac{1}{\Omega k_B T} \sum_p v \, (v \cdot \mathcal{F}) \, [E_{C0}(\mathbf{r}) + E(\mathbf{p}) - F_n(\mathbf{r})] \tau_f(\mathbf{p}) \left(-\frac{\partial f_S}{\partial \Theta} \right) \tag{2.29}$$

Substituting in Eq. 2.16 and writing the heat current in indicial notation

$$J_{Qi} = w_{ij}\partial_j(F_n/q) + K_{ij}\partial_j\left(\frac{1}{T}\right), \tag{2.30}$$

where

$$w_{ij} = \frac{-q}{\Omega k_B T}\sum_p v_i v_j \tau_f(\mathbf{p})[E_{C0}(\mathbf{r}) + E(\mathbf{p}) - F_n(\mathbf{r})]\left(-\frac{\partial f_S}{\partial \Theta}\right) \tag{2.31}$$

$$K_{ij} = \frac{-q}{\Omega k_B}\sum_p v_i v_j \tau_f(\mathbf{p})[E_{C0}(\mathbf{r}) + E(\mathbf{p}) - F_n(\mathbf{r})]^2\left(-\frac{\partial f_S}{\partial \Theta}\right) \tag{2.32}$$

The sums over momentum define the material parameters $\sigma_{ij}, B_{ij}, w_{ij}$, and K_{ij}. Equations 2.24 and 2.30 give the components of vector coupled current equations. The coupled current equations describe how current and heat flow within a material.

2.2 Using the Coupled Current Equations

2.2.1 The General Equations

Equations 2.24 and 2.30 describe the electrical current and heat current in terms of the material coefficients σ_{ij}, w_{ij}, B_{ij}, and K_{ij}, and the generalized forces $\partial_j(F_n/q)$ and $\partial_j(1/T)$. The four material coefficients can be calculated from the material properties: Fermi energy, band structure, scattering coefficient, etc. These calculations are beyond the scope of this thesis, and examples for some semiconductors can be found in Lundstrom [5].

The two coupled current equations 2.24 and 2.30 can be recast in a form more useful for comparisons with experiments. Here the forces are changed from the gradient of the electrochemical potential per unit charge to the gradient of the electric potential or minus the electric field

$$\partial_j(F_n/q) = \nabla(F_n/q) \approx \nabla V = -\mathbf{E}. \tag{2.33}$$

Similarly, $\partial_j(1/T)$ is written in terms of the temperature gradient

$$\partial_j(1/T) = \nabla(1/T) = -\frac{1}{T^2}\nabla T. \tag{2.34}$$

With these substitutions, the coupled current equations become

$$\mathbf{J} = [\sigma]\mathbf{E} - [\sigma][S]\nabla T \tag{2.35}$$

$$\mathbf{J}_Q = [\Pi]\mathbf{J} - [\kappa]\nabla T. \tag{2.36}$$

where $[\sigma]$ is the electrical conductivity tensor, $[S]$ is the Seebeck tensor, $[\Pi]$ is the Peltier coefficiant tensor, and $[\kappa]$ is the thermal conductivity tensor. Note that quantities in square brackets are tensors, and bold face symbols indicate vectors. The connections between these four coefficients (σ, S, Π, *and* κ) and those used in Eqs. 2.24 and 2.30 (σ_{ij}, S_{ij}, Π_{ij}, *and* K_{ij}) are given in Lunstrom [5].

Left multiplying Eq. 2.35 by $[\sigma]^{-1} = [\rho]$, they take on the more useful laboratory form

$$\mathbf{E} = [\rho]\mathbf{J} - [S]\nabla T \tag{2.37}$$

$$\mathbf{J}_Q = [\Pi]\mathbf{J} - [\kappa]\nabla T. \tag{2.38}$$

Writing the equations by filling in all the matrices and vectors gives

$$\begin{bmatrix} E_x \\ E_y \\ E_z \end{bmatrix} = \begin{bmatrix} \rho_{xx} & \rho_{xy} & \rho_{xz} \\ \rho_{yx} & \rho_{yy} & \rho_{yz} \\ \rho_{zx} & \rho_{zy} & \rho_{zz} \end{bmatrix} \begin{bmatrix} J_x \\ J_y \\ J_z \end{bmatrix} - \begin{bmatrix} S_{xx} & S_{xy} & S_{xz} \\ S_{yx} & S_{yy} & S_{yz} \\ S_{zx} & S_{zy} & S_{zz} \end{bmatrix} \begin{bmatrix} \partial_x T \\ \partial_y T \\ \partial_z T \end{bmatrix} \tag{2.39}$$

$$\begin{bmatrix} J_x^Q \\ J_y^Q \\ J_z^Q \end{bmatrix} = \begin{bmatrix} \Pi_{xx} & \Pi_{xy} & \Pi_{xz} \\ \Pi_{yx} & \Pi_{yy} & \Pi_{yz} \\ \Pi_{zx} & \Pi_{zy} & \Pi_{zz} \end{bmatrix} \begin{bmatrix} J_x \\ J_y \\ J_z \end{bmatrix} - \begin{bmatrix} \kappa_{xx} & \kappa_{xy} & \kappa_{xz} \\ \kappa_{yx} & \kappa_{yy} & \kappa_{yz} \\ \kappa_{zx} & \kappa_{zy} & \kappa_{zz} \end{bmatrix} \begin{bmatrix} \partial_x T \\ \partial_y T \\ \partial_z T. \end{bmatrix} \tag{2.40}$$

For isotropic materials all the parameter tensors become diagonal and simplify to

$$\begin{aligned} \Pi_{ij} &= \Pi_0\, \delta_{ij} \\ \rho_{ij} &= \rho_0\, \delta_{ij} \\ \kappa_{ij} &= \kappa_0\, \delta_{ij} \\ S_{ij} &= S_0\, \delta_{ij}. \end{aligned}$$

with the Kronecker delta δ_{ij} notation. For the most general anisotropic materials the off diagonal elements are not zero, and all the elements in Eq. 2.39 and Eq. 2.40 must be accounted for. Further explanation of the tensorial elements as related to the transverse thermoelectric effects of the devices modeled follows.

2.2.2 Transverse Thermoelectric Geometry

Isotropic thermoelectric materials produce the well-studied longitudinal Seebeck and Peltier effects. Anisotropic materials have a crystal structure that directs phenomena in different directions and produces transverse thermoelectric effects (TTE). It has been shown that anisotropy can be synthetically produced in multilayered, repeated stacks of two materials as shown in Fig. 2.1. After the materials are cut and pressed into a multilayered stack, the stack is rotated and cut at an angle α. The anisotropy comes from the differing parallel and perpendicular components of the materials' properties [6] as well as rotation. Materials A and B alternate in the stack and are usually a metal and semiconductor paired such that the materials' parameters provide sufficient magnitudes in the off diagonal elements to see TTE.

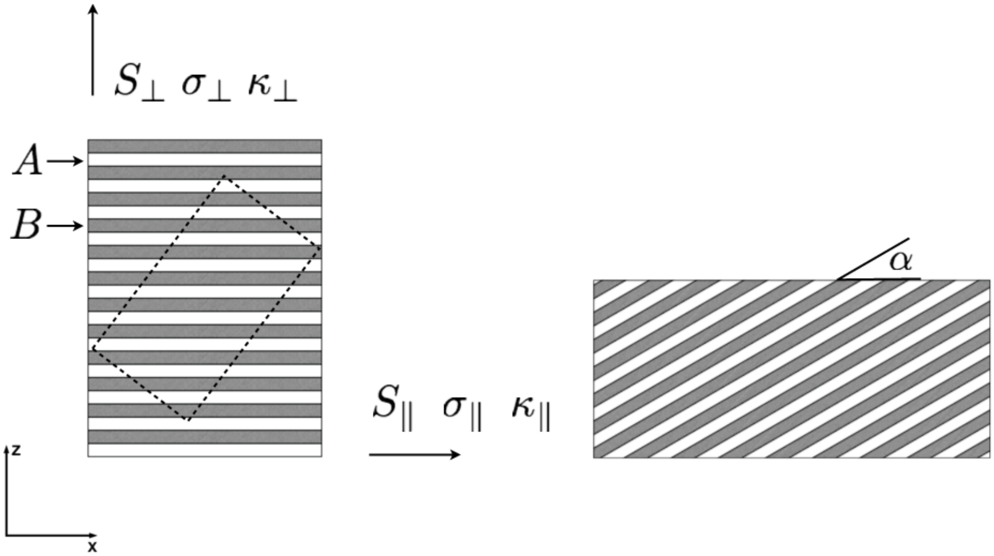

Figure 2.1: Geometry of a synthetically created anisotropic thermoelectric device with parallel and perpendicular components of material parameters shown.

The perpendicular and parallel components of the parameters are added in series and parallel, respectively, to get [6] [7]

$$S_{\parallel} = \frac{S_A\sigma_A + pS_B\sigma_B}{\sigma_A + p\sigma_B} \tag{2.41}$$

$$S_{\perp} = \frac{S_A\kappa_B + pS_B\kappa_A}{p\kappa_A + \kappa_B} \tag{2.42}$$

$$\kappa_{\perp} = \frac{\kappa_A\kappa_B(p+1)}{p\kappa_A + \kappa_B} \tag{2.43}$$

$$\kappa_{\parallel} = \frac{\kappa_A + p\kappa_B}{(p+1)} \tag{2.44}$$

$$\sigma_{\perp} = \frac{\sigma_A\sigma_B(p+1)}{p\sigma_A + \sigma_B} \tag{2.45}$$

$$\sigma_{\parallel} = \frac{\sigma_A + p\sigma_B}{(p+1)}, \tag{2.46}$$

where p is the ratio of layer thicknesses t_B/t_A. Rotating around the y-axis as shown in Fig. 2.1, the tensors have the general form [7]

$$[T] = \begin{bmatrix} T_{\parallel}cos^2(\alpha) + T_{\perp}sin(\alpha)^2 & 0 & \left(T_{\parallel} - T_{\perp}\right)\frac{1}{2}sin(2\alpha) \\ 0 & T_{\parallel} & 0 \\ \left(T_{\parallel} - T_{\perp}\right)\frac{1}{2}sin(2\alpha) & 0 & T_{\parallel}sin^2(\alpha) + T_{\perp}cos^2(\alpha) \end{bmatrix} \tag{2.47}$$

Both the parallel and perpendicular components are set upon determination of the materials being used in the stack. On inspection of the off diagonal components, it is seen that the maximum anisotropy occurs when the tilt angle α is 45°. The T_{yy} component is unaffected by the rotation. The T_{xx} and T_{zz} components are sums of $T_{\perp}$ and $T_{\parallel}$. Upon rotation each term in the sum of the T_{xx} and T_{zz} components are scaled by either $Sin^2(\alpha)$ or $Cos^2(\alpha)$. In words T_{xx} and T_{zz} switch places during the rotation from 0° to 90°.

Going back to equations 2.39 and 2.40 and performing the correct rotations on each parameter's matrix, we have the set of simultaneous equations

$$E_x = J_x\rho_{xx} + J_z\rho_{xz} - S_{xx}\frac{\partial T}{\partial x} - S_{xz}\frac{\partial T}{\partial z} \tag{2.48}$$

$$E_y = J_y\rho_{yy} \tag{2.49}$$

$$E_z = J_x\rho_{zx} + J_z\rho_{zz} - S_{zx}\frac{\partial T}{\partial x} - S_{zz}\frac{\partial T}{\partial z} \tag{2.50}$$

$$J_x^Q = J_xS_{xx}T + J_zS_{xz}T - \kappa_{xx}\frac{\partial T}{\partial x} - \kappa_{xz}\frac{\partial T}{\partial z} \tag{2.51}$$

$$J_y^Q = J_yS_{yy}T \tag{2.52}$$

$$J_z^Q = J_xS_{zx}T + J_zS_{zz}T - \kappa_{zx}\frac{\partial T}{\partial x} - \kappa_{zz}\frac{\partial T}{\partial z}. \tag{2.53}$$

In the equations above, it is assumed there is no temperature gradient in the y direction, $\partial T/\partial y = 0$, and that the xy, yx, yz, and zy components of all three transport tensors are zero as seen in Eq. 2.47. Equations 2.48 - 2.53 reveal some interesting effects in transverse thermoelectric devices.

2.3 Open Circuit Eddy Currents

Thermoelectric eddy currents are described in references [8], [9], [10], and [11]. Upon inspection of the current densities, it was seen that they are not zero even though the Seebeck simulations had no input current boundary condition. In other words eddy currents are generated in open circuit conditions. Thermoelectric eddy currents manifest in two types of materials: anisotropic materials and inhomogeneous materials. A surface perpendicular electric field $E_\perp$ is generated due to the discontinuity of the Seebeck coefficient in each of the alternating layers [10].

Maxwell's equations always provide the starting point in investigations of electrical effects. With $\mathbf{B} = 0$ Faraday's Law tells us that

$$\nabla \times \mathbf{E} = -\frac{\partial \mathbf{B}}{\partial t} = 0 \tag{2.54}$$

$$\nabla \times \mathbf{E} = \nabla \times ([\rho]\mathbf{J} - [S]\nabla T) = 0 \tag{2.55}$$

$$\nabla \times ([\rho]\mathbf{J}) = \nabla \times ([S]\nabla T) \tag{2.56}$$

Due to the anisotropy of the Seebeck tensor the right hand side of Eq. 2.56 will not be zero as stated in Anatychuk [12]. Necessarily, then, the left hand side cannot be zero, and thermoelectric eddy currents must be generated.

2.4 Finite Element Method

COMSOL Multiphysics uses the finite element method (FEM) to compute numerical solutions. The FEM has the extremely advantageous property that it can be used for complicated geometries unlike the finite difference method (FDM). FEM also handles discontinuities like abrupt material parameter changes well since the domain is split into smaller, local subdomains. These aspects of FEM makes it the numerical method of choice for many applications such as heat flow or structural stress simulations. The 6 steps in applying the FEM as outlined in Lewis et al. [13] are

1. Discretize the continuum

2. Select interpolation or shape functions

3. Form element equations
4. Assemble the element equations to obtain a system of simultaneous equations
5. Solve the system of equations
6. Calculate the secondary quantities

With the exception of step 3, COMSOL Multiphysics software handles these tasks. So, the equations that govern the thermoelectric effect, e.g. the coupled current equations, needed to be implemented in the correct way in order to have the FEM converge on a correct solution. Implementation of these equations is outlined in the Physics Builder Guide [14] and is shown here. It is a straight forward task to generalize to the equations to suit anisotropy. However, to simplify the notation the coefficients here are scalars. The defining equations for a thermoelectric system are

$$\mathbf{E} = \rho\mathbf{J} + S\nabla T \tag{2.57}$$

$$\mathbf{J}_Q = \Pi\mathbf{J} - \kappa\nabla T \tag{2.58}$$

$$\mathbf{E} = -\nabla V \tag{2.59}$$

$$Q = \mathbf{J} \cdot \mathbf{E}, \tag{2.60}$$

where the definitions of symbols are

$\mathbf{J} \equiv current\ density\ (A/m^2)$

$\mathbf{J}_Q \equiv heatflux\ density\ (W/m^2)$

$\mathrm{S} \equiv Seebeck\ coefficient\ (\mu V/K)$

$\rho \equiv electrical\ resistance\ (\Omega \cdot m)$

$\mathbf{E} \equiv electric\ field\ (V/m)$

$\sigma \equiv electrical\ conductivity\ (1/\Omega m)$

$\Pi \equiv Peltier\ coefficient$

$\kappa \equiv thermal\ conductivity\ (W/m \cdot K)$

$\mathrm{T} \equiv absolute\ temperature\ (K)$

$\mathrm{Q} \equiv Joule\ heating\ (J)$

$\mathrm{V} \equiv electric\ potential (V)$

$\nabla \equiv differential\ operator$

Table 2.1: Symbol Definitions

Energy and charge conservation give the time dependent equations:

$$\rho C \frac{\partial T}{\partial t} + \nabla \cdot \mathbf{J}_Q = Q \tag{2.61}$$

$$\nabla \cdot \mathbf{J} = -\frac{\partial \rho_c}{\partial t} \tag{2.62}$$

where ρ is the density, C is the heat capacity, and ρ_c is the charge density. The stationary case is implemented in COMSOL, and in this case they simplify to

$$\nabla \cdot \mathbf{J}_Q = Q \tag{2.63}$$

$$\nabla \cdot \mathbf{J} = 0. \tag{2.64}$$

Implementation of the FEM requires that equations be put into weak form. Weak forms of equations hold true over a locally defined domain instead of over an infinite domain. Over this local domain weak solutions are found with respect to a set of interpolation functions, also called basis functions. These basis functions are not orthogonal since intersecting elements contain the some of the same nodes. This is one of the differences between the FEM and FDM. In FDM the governing functions are approximated while the basis functions are orthogonal. In FEM the governing functions are global while the basis functions are approximated. The basis functions are represented with v_T and v_V. T and V are the dependent variables for the *Temperature* and the *Electric Potential*, respectively, for which the FEM solution defines. The volume integrals are over the local domain over which the equations are assumed to hold true in the weak formulation. The surface area integrals are the boundary surfaces that define the limits of the local domains.

Weak Form of Heat Equation

$$\iiint (\nabla \cdot \mathbf{J}_Q) v_T \, d\tau = \iiint Q \, v_T \, d\tau \tag{2.65}$$

$$-\iiint \mathbf{J}_Q \cdot \nabla v_T \, d\tau + \oiint (\mathbf{n} \cdot \mathbf{J}_Q) v_T \, dA = \iiint Q v_T \, d\tau \tag{2.66}$$

$$-\iiint \mathbf{J}_Q \cdot \nabla v_T \, d\tau + \oiint J_{Q0} \, v_T \, dA = \iiint Q v_T \, d\tau \tag{2.67}$$

Weak Form of Current Equation

$$\iiint (\nabla \cdot \mathbf{J}) v_V \, d\tau = 0 \tag{2.68}$$

$$-\iiint \mathbf{J} \cdot \nabla v_V \, d\tau + \oiint (\mathbf{n} \cdot \mathbf{J}) v_V \, dA = 0 \tag{2.69}$$

$$-\iiint \mathbf{J} \cdot \nabla v_V \, d\tau + \oiint J_0 \, v_V \, dA = 0 \tag{2.70}$$

Implementation of the coupled current equations in these integral forms allow COMSOL to compute solutions inside the customized transverse thermoelectric physics modules built. The steps followed for the simulations are described in the next chapter.

Chapter 3

Simulations

3.1 COMSOL Transverse Thermoelectric Package

3.1.1 COMSOL Physics Builder

The COMSOL Multiphysics software does not have a thermoelectric module available in the basic software package nor is there one to purchase. There is, however, documentation on how to create a custom physics interface which defines the steps needed to create custom modules for any physical system. The *Physics Interface Builder User's Guide* [14] also provides the information necessary to customize existing physics modules to suit any situation that may not be accounted for in a market ready module available. There are two example implementations provided in the documentation, the "Thermoelectric Effect" and the "Schrodinger Equation" examples. The "Thermoelectric Effect" example demonstrates how to build a longitudinal thermoelectric module (LTM) for traditional longitudinal thermoelectric effect device simulations. In order to convert this package to account for the transverse thermoelectric effect some modifications needed to be implemented.

3.1.2 Modifying the Thermoelectric Module

The decision was made to build two models to compare results and determine what, if any, discrepancies occurred between the two models. One model is completely mathematical and follows the theory of simulated anisotropic devices originally introduced by Babin, et al. in 1974 [15]. This model is hereto referred to as the *anisotropic slab model* (ASM). The other model is an *isotropic layer model* (ILM) consisting of layers using isotropic material parameters, and simulations consisted of building the CAD models similar to those outlined in Babin et al [15]. Both interface models were built for a steady state simulation.

After building the longitudinal thermoelectric module, certain modifications needed to be implemented in order to obtain accurate results for the ILM transverse thermoelectric effect. The first modification was simply to make the Seebeck coefficient available as a variable parameter to any type of material such that it was defined to be used in computations. This required creating a custom material property group. Each material added to the model, then, had to be created in conjunction with this material property group in order for COMSOL to perform the needed calculations. In order to model the Peltier effect, the electric current boundary condition needed to be added to the model such that an input of current was possible. Since the electric current boundary term was set to zero in the *Physics Interface Builder User's Guide* LTM instructions, this modification required an implementation of the weak form of the electric current equation. The same steps were followed as outlined for the heat flux boundary conditions in the *Physics Interface Builder User's Guide*. This CAD model shown in Fig. 3.1 used in conjunction with the ILM is a true representation of an artificially anisotropic device that can be constructed. This model is studied in parallel with the ASM detailed next.

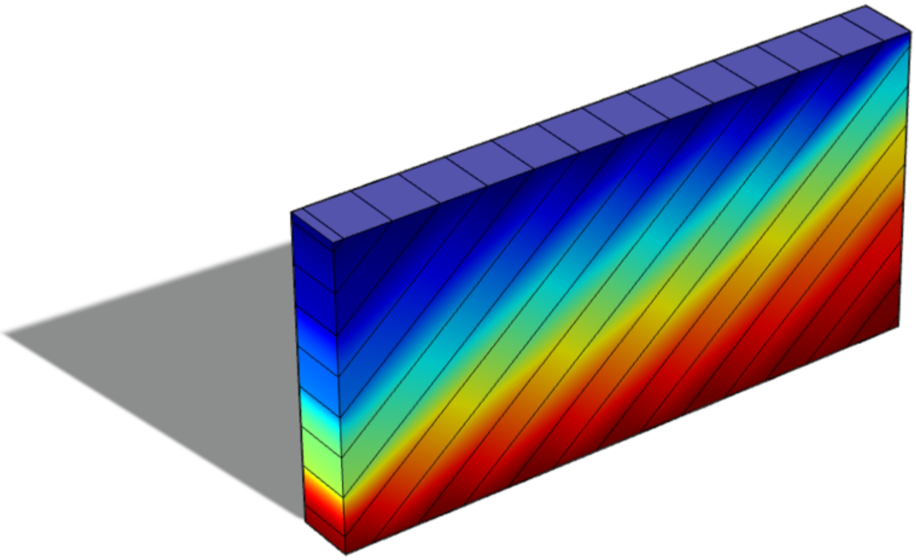

Figure 3.1: CAD model of a device made using the isotropic layer model where the layers are apparent.

In order to create the ASM, the thermoelectric equations had to be generalized as outlined in the background chapter of this thesis. The material parameters that were defined as scalars in the LTM are now defined as tensors for the ASM. Simple multiplication was converted to inner products where the tensorial material parameters were multiplied with vectors and/or other tensors. When a tensor was multiplied by a constant, regular multiplication was used such as in the calculation of the Peltier coefficient $\Pi = [S] \cdot T$. In this case $[S]$ is the Seebeck tensor, and T is the absolute temperature, a scalar. As can be seen in comparison with the ILM, the ASM CAD model shown in Fig. 3.2 is purely a mathematical model as there are no discontinuities in regards to surface to surface material parameter discontinuities. As explained later it turns out that this is an important difference in the models.

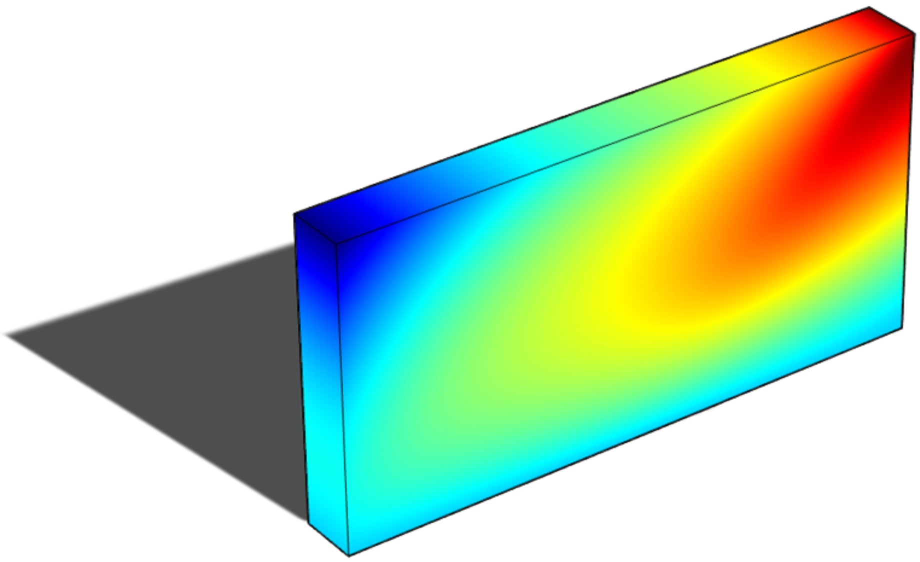

Figure 3.2: CAD model of a device made using the anisotropic slab model where the continuity of the geometry implies the purely mathematical nature of the model.

3.2 Validation Simulations

In order to verify that the ILM and the ASM were built properly and calculated the correct results, two papers were used as bases for verification. Zahner's paper [16] experimentally determined a transverse voltage with a constant heat flux input across a surface. Kyarad and Lengfellner [6] measured the transverse temperature difference while varying the input current. Using these two papers allowed for verification of each TTE model for each of the thermoelectric phenomena.

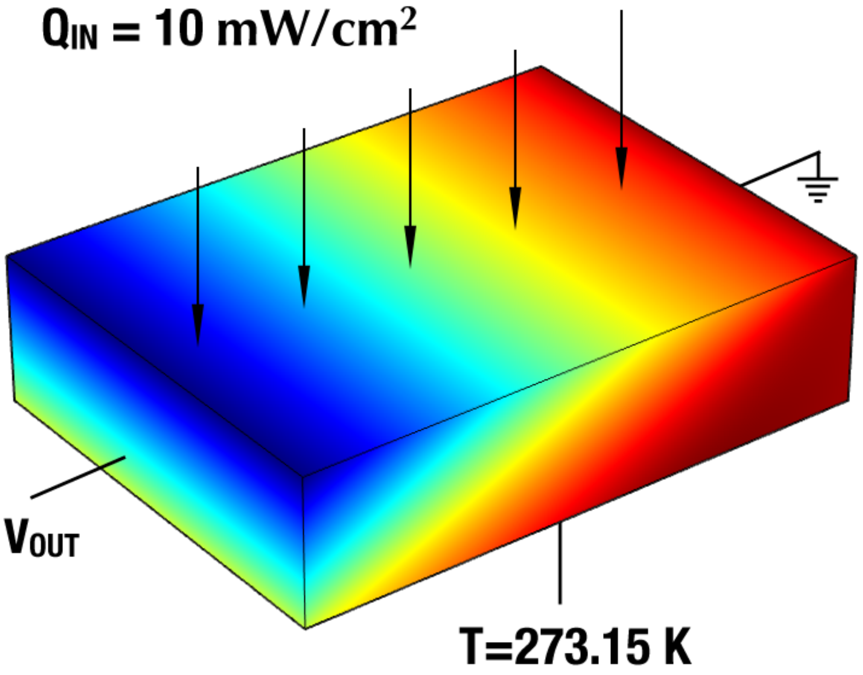

Figure 3.3: Experimental set up in Zahner et al. [16] with constant heat flux applied to sample top, the bottom face held at constant temperature, and potential difference calculated from left to right.

Using both the ILM and the ASM, Zahner, et al. [16] device dimensions were built using the CAD software that was included with the basic COMSOL package. The dimensions were 8mm, 6mm, 2mm for the length, width, and height respectively. A constant heat flux density of $10(mW/cm^2)$ was input across the top surface while the angle of inclination of the layers was varied. The geometry of the experiment can be seen in Fig. 3.3 [16]. As can be seen in the plot of the data obtained in both models in Fig. 3.4 as well as the data in Zahner et al. [16], there is a close agreement between experiment and simulation of the Seebeck effect for this device. It was determined that each of the physics interfaces built were sufficiently accurate to continue with a computational analysis of the Seebeck effect.

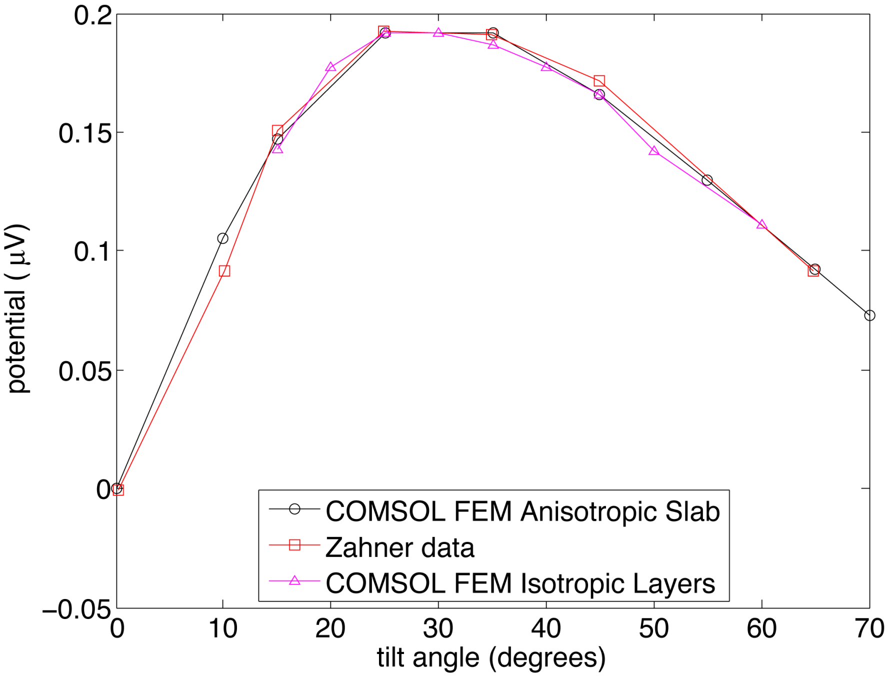

Figure 3.4: Validation of the physics modules with the data in measured in Zahner et al. [16] for both ILM and ASM.

The paper by Kyarad and Lengfellner [6] was used as the basis in the validation process for the Peltier effect. As stated in their paper, the experiment's boundary conditions were not kept constant. It is stated that, ”the sample bottom is heated above the coolant temperature due to insufficient thermal coupling.” [6] Therefore, without adding this heat flux into the simulation, a difference in computations and measured data was expected. The experimental set up is pictured in Fig. 3.5 [6].

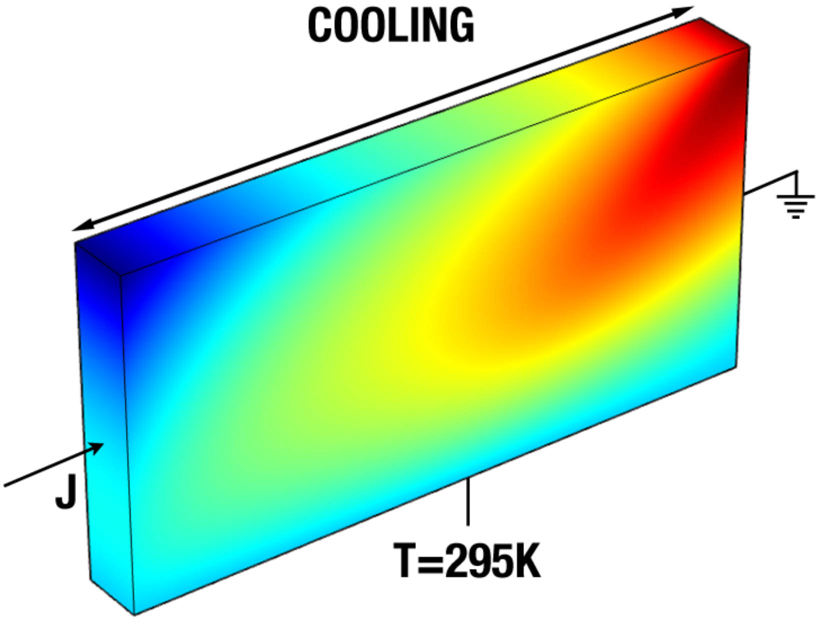

Figure 3.5: Experimental set up in Kyarad et al. [6] in which a current is injected into the left face, and Peltier cooling occurs across the top of the device with the bottom face kept at constant temperature.

In a paper by Ali, et al. [17] different heat fluxes were implemented to simulate the heat transfer that was mentioned in the paper by Kyarad, et al [6]. Although some qualitative aspects were seen in the simulations, the simulations were unsuccessful in matching the measured data. The same parabolic qualitative aspects of the data were seen in the COMSOL computations. COMSOL computations were measured at the midpoint of the sample. A surface average was also computed across the entire top surface where the cooling occurred. It turns out that the midpoint and the surface average are quite close, and both computations are plotted along with the Kyarad data in Fig. 3.6 [6]. As expected the discrepancy between the COMSOL adiabatic boundary conditions and the measured data is apparent. The ILM did not converge with the ASM as it did in computing the Seebeck effect. The difference between the two models was investigated and is explained in section 4.2.

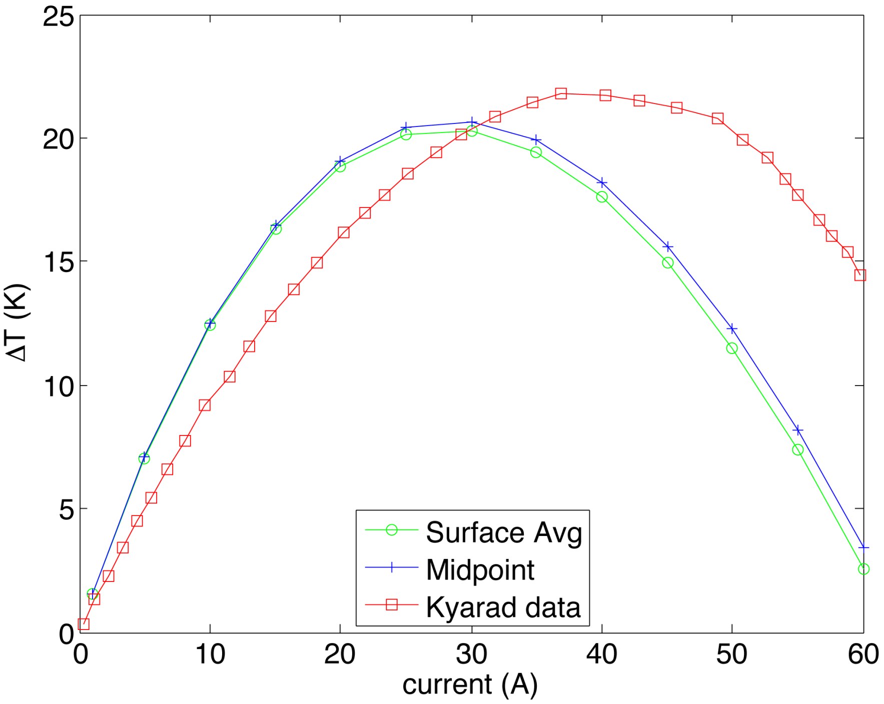

Figure 3.6: Validation of the physics modules with the data in measured in Kyarad et al. [6] for the ASM using the midpoint computation as well as the surface average.

3.3 Transverse Seebeck Effect

The transverse Seebeck effect occurs when a temperature difference is applied in the z-direction a potential difference occurs in the x-direction as in Fig. 3.7. In order to study the transverse Seebeck effect various boundary conditions and geometries were built in the ILM and ASM. The geometry varied in aspect ratios for $\Delta x/\Delta z < 1$ and $\Delta x/\Delta z > 1$. The angle of inclination ranged from 0 to $\pi/2$.

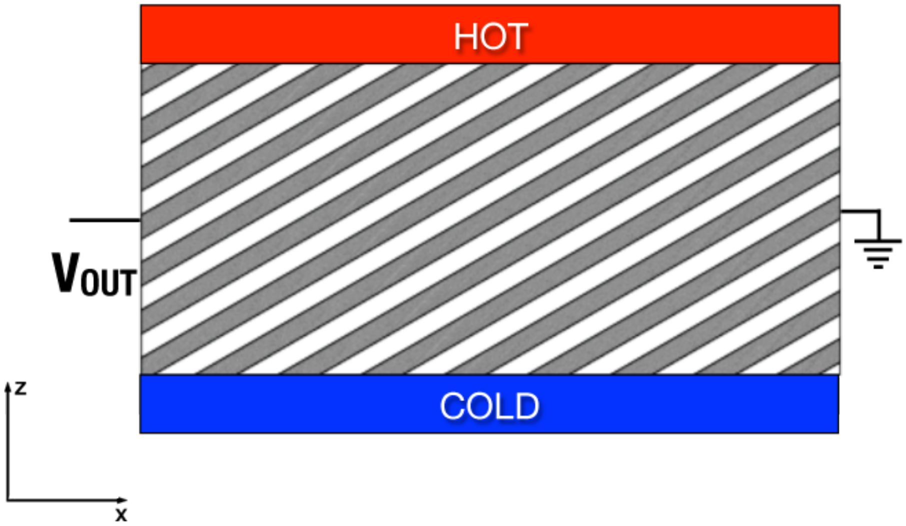

Figure 3.7: Diagram of the transverse Seebeck effect simulation where a temperature difference is in z-direction, and the potential difference is calculated in the x-direction.

With a temperature difference applied in the z-direction, a transverse potential difference is generated in the x-direction. Looking at the x component of the electrical current equation along with the open circuit condition gives us the electric field.

$$E_x = \rho_{xx} J_x + \rho_{xz} J_z - S_{xx}\frac{\partial T}{\partial x} - S_{xz}\frac{\partial T}{\partial z} = -\nabla_x V \tag{3.1}$$

Integrating along the x-direction will give the potential

$$V_L - V_0 = -\int_0^L E_x dx = -\int_0^L \left(\rho_{xx} J_x + \rho_{xz} J_z + S_{xx}\frac{\partial T}{\partial x} + S_{xz}\frac{\partial T}{\partial z}\right) dx \tag{3.2}$$

$$V_L - V_0 = \int_0^L S_{xx}\frac{\partial T}{\partial x} dx + \int_0^L S_{xz}\frac{\partial T}{\partial z} dx - \int_0^L \left(\rho_{xx} J_x + \rho_{xz} J_z\right). \tag{3.3}$$

It mat be assumed that J_x and J_z are zero since there is an open circuit condition applied to the device; however, eddy currents occur in the simulations. The effects are smaller than the Seebeck thermopotential components of the sum but are not negligible. The last integral in Eq. 3.3 must be taken into account as it subtracts from the thermopotential. However, a qualitative understanding of the thermopotential's dependence on aspect ratio can be achieved by looking at the first two terms in Eq. 3.3.

$$V_L - V_0 \approx \int_0^L S_{xx}\frac{\partial T}{\partial x} dx + \int_0^L S_{xz}\frac{\partial T}{\partial z} dx. \tag{3.4}$$

This equation depends on the temperature gradient components in the x and z directions, $\partial T/\partial x$ and $\partial T/\partial z$ respectively. These quantities take on a parabolic nature, but for a qualitative understanding, they can be approximated with

$$\frac{\partial T}{\partial z} \approx \frac{T_h - T_c}{d} \quad \mathit{and} \quad \frac{\partial T}{\partial x} \approx \frac{T_L - T_0}{L}, \tag{3.5}$$

where T_h and T_c are the constant applied boundary conditions in the z-direction. T_L is the temperature at $x = L$, and T_0 is the temperature at $x = 0$. Substituting these expressions into the integrals

$$V_L - V_0 \approx S_{xx} \left(\frac{T_L - T_0}{L} \right) \int_0^L dx + S_{xz} \left(\frac{T_h - T_c}{d} \right) \int_0^L dx \tag{3.6}$$

$$V_L - V_0 \approx S_{xx} \left(T_L - T_0 \right) + S_{xz} \left(T_h - T_c \right) \left(\frac{L}{d} \right) . \tag{3.7}$$

The dependence on the aspect ratio (L/d) is explicit in the approximation. A device that is longer will produce a higher potential difference. It turns out that the potential adds in series along the transverse direction. A longer device will have a higher potential, all other conditions unchanged, but there is a loss mechanism at play. There is no current input through the device in this study, but eddy currents form as shown in Eq. 2.56. As discussed below the eddy currents form to the detriment of the thermopotential created in the device.

3.4 Transverse Peltier Effect

The transverse Peltier effect occurs when a current is applied to a device in one direction, and cooling occurs on one side of the device in a direction perpendicular to the flow of current. Fig. 3.8 illustrates this configuration for current in the x-direction and cooling in the z-direction. In this study the current was varied from 1 Amp to as high as 80 Amps in some simulations in order to find the maximum amount of cooling that could occur.

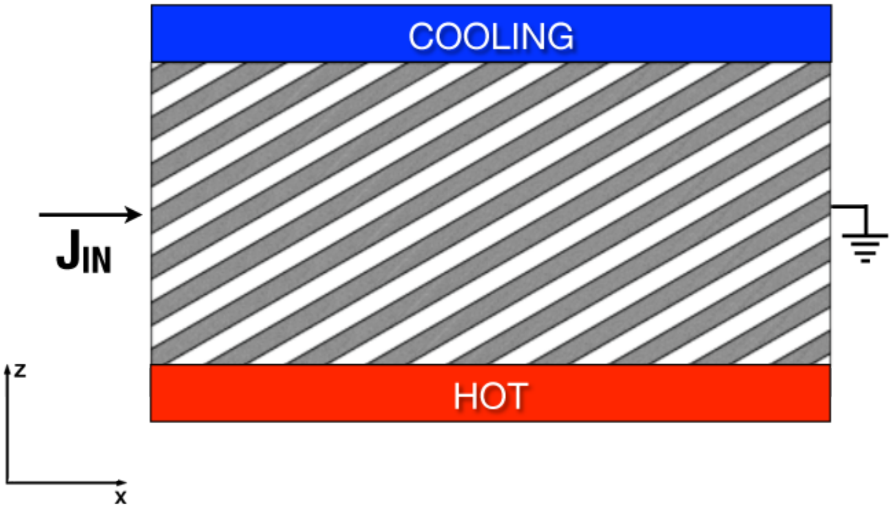

Figure 3.8: Diagram of the transverse Peltier effect simulation where a current is injected in the z-direction, and heat flows in z-direction to cool off the top plate.

In the simulations the conditions for the y-component of heat flow are no current in the y-direction $J_y = 0$ as well as no temperature difference $\partial T/\partial y = 0$. Consequently, there is no heat flow in the y-direction $J_y^Q = 0$ by Eq. 2.52. The equations governing the heat flow in a transverse thermoelectric device are then

$$J_x^Q = J_x S_{xx} T + J_z S_{xz} T - \kappa_{xx} \frac{\partial T}{\partial x} - \kappa_{xz} \frac{\partial T}{\partial z} \tag{3.8}$$

$$J_z^Q = J_x S_{zx} T + J_z S_{zz} T - \kappa_{zx} \frac{\partial T}{\partial x} - \kappa_{zz} \frac{\partial T}{\partial z}. \tag{3.9}$$

J_z is not zero as we get an electric field component from 2.50 directing some current in the z-direction.

$$E_z = J_x \rho_{zx} + J_y \rho_{zy} + J_z \rho_{zz} - S_{zx} \frac{\partial T}{\partial x} - S_{zz} \frac{\partial T}{\partial z} \tag{3.10}$$

So, both J_x and J_z contribute to the heat flux. Joule heating is accounted for in the weak form equations input for the FEM solver in COMSOL. This opposes Peltier cooling in some cases as described below in the results section.

Chapter 4

Results

4.1 Transverse Seebeck Effect

4.1.1 Aspect Ratio and Output Voltage

A simple analysis of the coupled current equations reveals how the output voltage depends on the aspect ratio. This understanding is important in order to maximize the thermopower for geometric constraints of a device needed in a specified circuit. After confirming the validity of the models, the models were compared more thoroughly to determine if there was a point at which either broke down. Any differences in the two models also needed to be known to account for any discrepancies in calculations output by the simulations.

Voltage Profiles

Examining the potential drops across a device given a certain temperature difference, we see in Fig. 4.1 that the two models have a predictable difference. The ASM is a mathematical idealization while the ILM has a discrete nature due to the layers' interfaces throughout the model. As a consequence the ASM has smoother profiles than does the ILM.

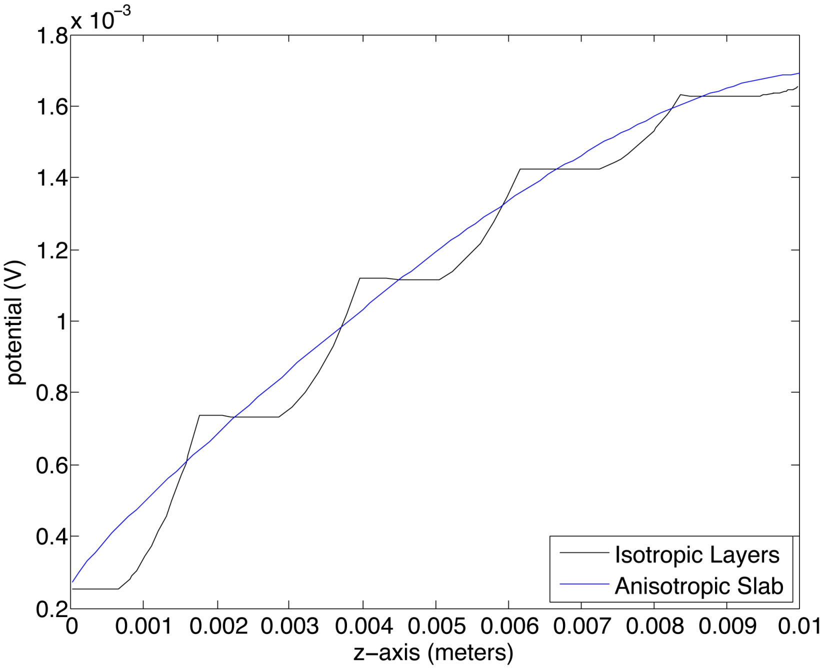

Figure 4.1: Difference in voltage drop profile across z-axis for the ASM and ILM in a Seebeck effect simulation.

4.1.2 Angle of Inclination and Aspect Ratio

With the two models in close agreement with experiment, the Seebeck effect was investigated further. Using adiabatic boundary conditions a temperature difference was set in the z-direction and a potential difference calculated in the x-direction. The bottom surface was kept at 273.15K while the top surface was held at 263.13K. The aspect ratio $\Delta x/\Delta z$ was varied in the x-direction to determine what, if any, effect this would have on the output transverse voltage. For each of the varying aspect ratios, the of angle of inclination was varied to see if there is a relationship between the two.

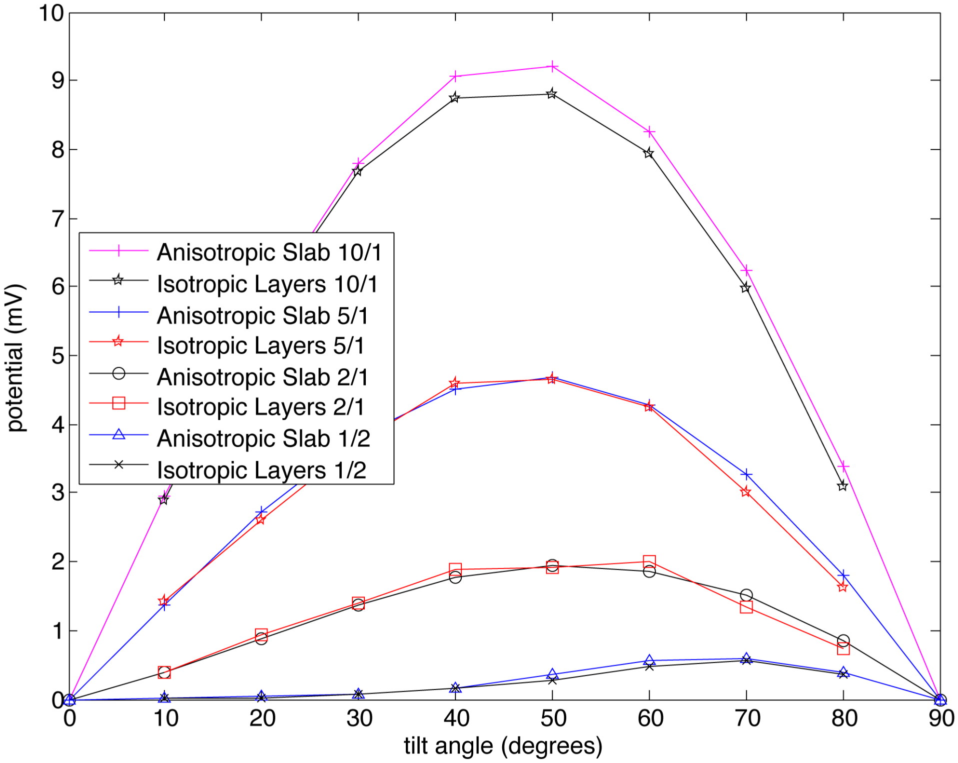

Figure 4.2: Seebeck effect model comparison of ILM and ASM for aspect ratios $\Delta x/\Delta z = (10, 5, 2, .5)$.

Fig. 4.2 implies that for the maximum output potential, there is a relationship between aspect ratio and angle of inclination. Along with a slight divergence at an aspect ratio of $\Delta x/\Delta z = 10$, the maximum output voltage migrates with changing aspect ratio. For longer devices the maximum voltage is produced closer and closer to an angle of 45°. Since the relationship between the electric field produced depends on the angle of inclination, we can find a function that maximizes both the potential and the electric field from the coupled current equations. Simply set the derivative equal to zero and then solve for the angle α.

Looking at the x component of the electric field equations and for the moment neglecting the eddy currents

$$E_x = -S_{xx}\frac{\partial T}{\partial x} - S_{xz}\frac{\partial T}{\partial z} = \frac{\partial V}{\partial x} \tag{4.1}$$

$$\frac{\partial E_x}{\partial \alpha} = \frac{\partial}{\partial \alpha}\left[S_{xx}\frac{\partial T}{\partial x} + S_{xz}\frac{\partial T}{\partial z}\right] = 0. \tag{4.2}$$

Plugging in our expressions for S_{xx} and S_{xz} after rotation, we have

$$\frac{\partial E_x}{\partial \alpha} = \frac{\partial}{\partial \alpha}\left[\left(S_{\parallel}cos^2(\alpha) + S_{\perp}sin(\alpha)^2\right)\frac{\partial T}{\partial x} - \left(S_{\parallel} - S_{\perp}\right)\frac{1}{2}sin(2\alpha)\frac{\partial T}{\partial z}\right] = 0 \tag{4.3}$$

$$\left(-2S_{\parallel}cos(\alpha)sin(\alpha) + 2S_{\perp}sin(\alpha)cos(\alpha)\right)\frac{\partial T}{\partial x} - \left(S_{\parallel} - S_{\perp}\right)cos(2\alpha)\frac{\partial T}{\partial z} = 0. \tag{4.4}$$

Now, simplifying

$$sin(2\alpha)\left(S_{\perp}-S_{\parallel}\right)\frac{\partial T}{\partial x}+\left(S_{\perp}-S_{\parallel}\right)cos(2\alpha)\frac{\partial T}{\partial z}=0 \tag{4.5}$$

$$sin(2\alpha)\left(S_{\perp}-S_{\parallel}\right)\frac{\partial T}{\partial x}=-\left(S_{\perp}-S_{\parallel}\right)cos(2\alpha)\frac{\partial T}{\partial z} \tag{4.6}$$

$$tan(2\alpha)=-\left(\frac{\partial T}{\partial z}\Big/\frac{\partial T}{\partial x}\right) \tag{4.7}$$

$$\alpha=\frac{1}{2}arctan\left[-\left(\frac{T_d-T_{z=0}}{d}\right)\Big/\left(\frac{T_L-T_{x=0}}{L}\right)\right] \tag{4.8}$$

$$\alpha=\frac{1}{2}arctan\left[-\left(\frac{T_d-T_{z=0}}{T_L-T_{x=0}}\right)\left(\frac{L}{d}\right)\right]. \tag{4.9}$$

$\left(S_{\perp}-S_{\parallel}\right)$ is never zero since $S_{\perp}$ and $S_{\parallel}$ will always have different values. While expression 4.9 is an approximation, the implicit dependence of the angle of inclination α on the aspect ratio $\Delta x/\Delta z = L/d$ seen in the simulations is affirmed.

4.1.3 Seebeck Tensor and Potential

As pointed out, the off diagonal term of the rotated Seebeck tensor S_{xz} reaches its maximum at 45°. Naturally the question arises as to why this occurs. An examination of the Seebeck coefficients provides some mathematical insight into what is happening. The Seebeck tensor components contributing in Eq. 4.1 are the S_{xx} and S_{xz} are, respectively,

$$S_{xx}=S_{\parallel}cos^2(\alpha)+S_{\perp}sin^2(\alpha) \tag{4.10}$$

$$S_{xz}=\frac{1}{2}\left(S_{\parallel}-S_{\perp}\right)sin(2\alpha). \tag{4.11}$$

Fig. 4.3 shows the components plotted for angles of inclination $0° - 90°$. It is clear that for angles higher than 45° the S_{xx} component has the higher magnitude. There is an important aspect as to what is happening to the components during the rotation: S_{xx} switches from $S_{\|}$ to $S_{\perp}$. So for devices with an aspect ratio less than 1, a higher angle of inclination will produce higher voltages.

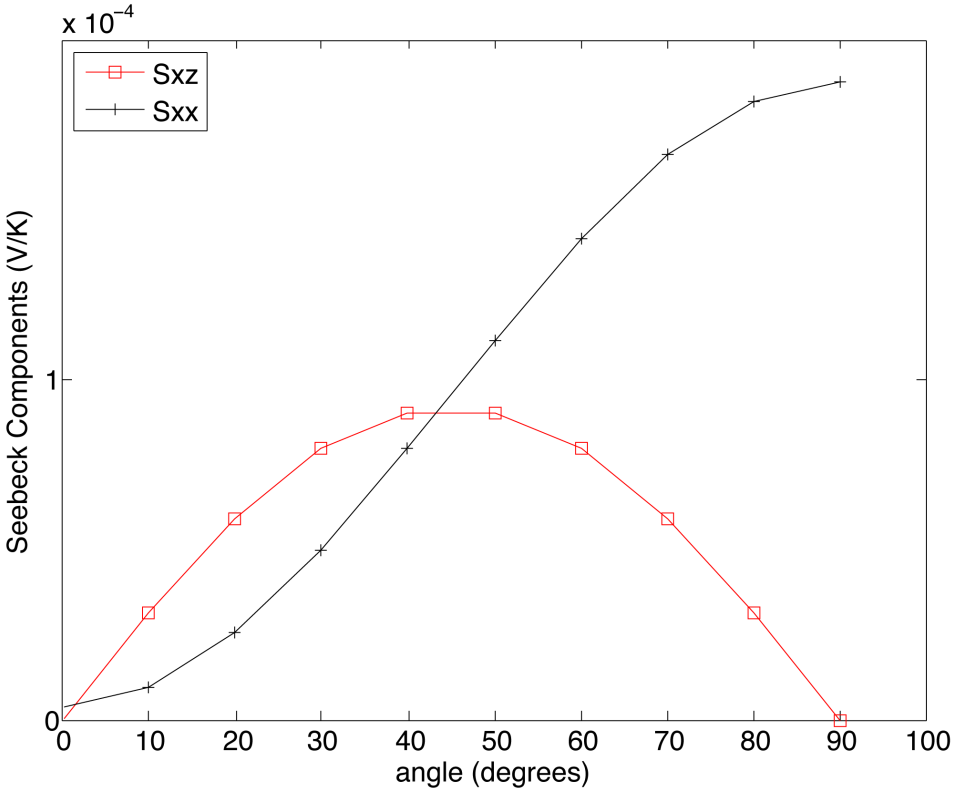

Figure 4.3: Magnitude of Seebeck components, S_{xz} and S_{zz} for angles of inclination 0°-90°.

The Seebeck components are scaled by the temperature gradients in the x and z directions. A line integral of the electric field through the middle of the block in the

ASM gives the potential across the block.

$$V = \int_0^L S_{xx}\frac{\partial T}{\partial x}dx + \int_0^L S_{xz}\frac{\partial T}{\partial z}dx - \int_0^L \left(\rho_{xx}J_x + \rho_{xz}J_z\right)dx. \tag{4.12}$$

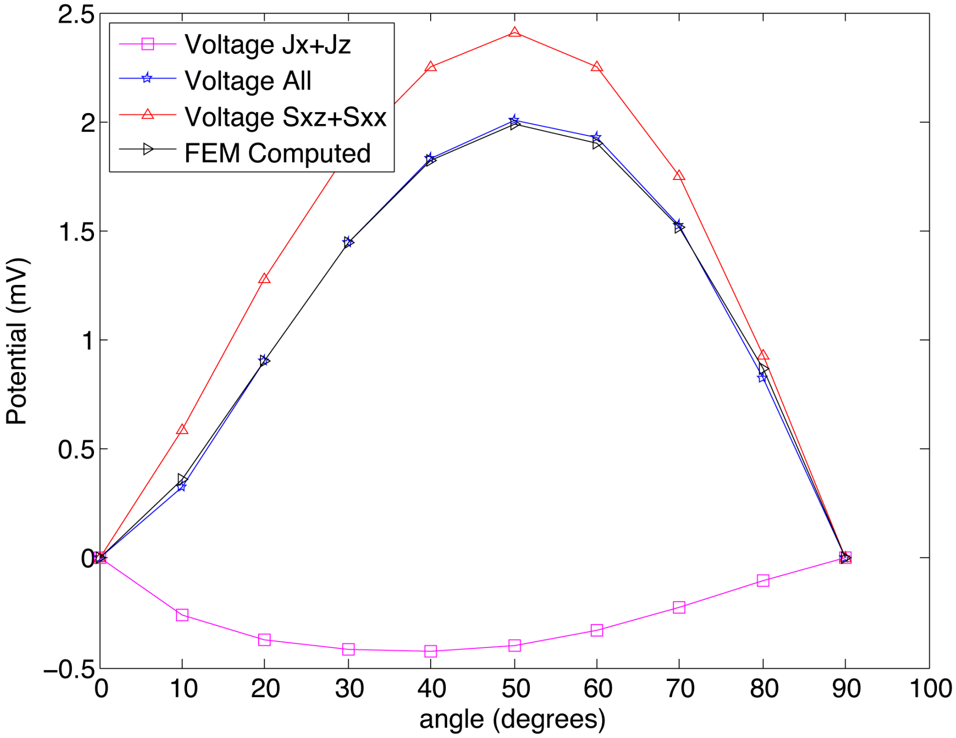

Figure 4.4: Magnitude of voltage components contributing to x component of the thermoelectric field for angles of inclination 0°-90°.

The integrals of the eddy current contributions, the Seebeck thermopotential contributions, the total potential, and the FEM solution are shown in Fig. 4.4. It was first assumed that J_x and J_z were zero since there was no current injected into the device. The line integral of the Seebeck contributions computed overshoots the FEM solution, so a reconsideration was necessary. As stated eddy currents arise, and so, J_x and J_z are not equal to zero and must be considered in the integral. It turns out that the eddy current contributions were precisely the difference needed to correct for the aforementioned assumption.

4.1.4 Eddy Currents in the ASM and ILM

Eddy currents must be taken into account for accurate understanding and modeling of the Seebeck effect in transverse thermoelectric devices. These currents take on different distributions for the ILM and ASM. The reason, as stated in Anatychuk and Luste [10], is due to the surface to surface interfaces in the ILM. Due to the jump discontinuities at each interface of the Seebeck coefficients, a surface perpendicular electric field component $E_\perp$ will contribute to the direction of the currents. Some similarities in the ILM and ASM are seen in the eddy current directions. The $E_\perp$ redirects some of the eddy currents in the ILM as can be seen in Figs. 4.5, 4.6, 4.7, and 4.8.

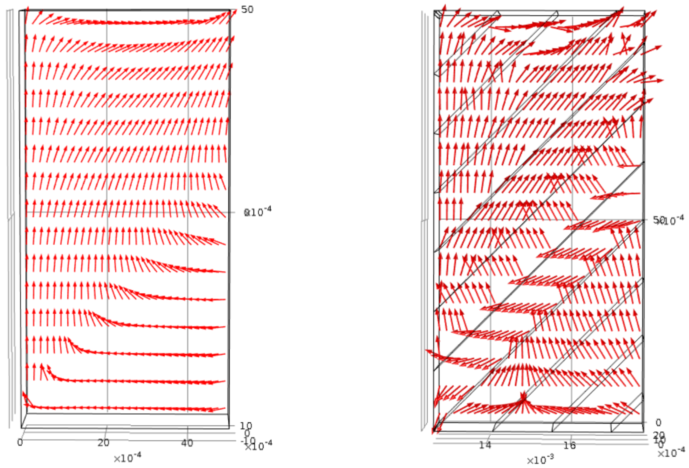

Figure 4.5: ASM (left) and ILM (right) shown with normalized eddy current densities for open circuit Seebeck potential at 45 degree angle of inclination, aspect ratio of 1/2, and ten degree temperature difference top to bottom.

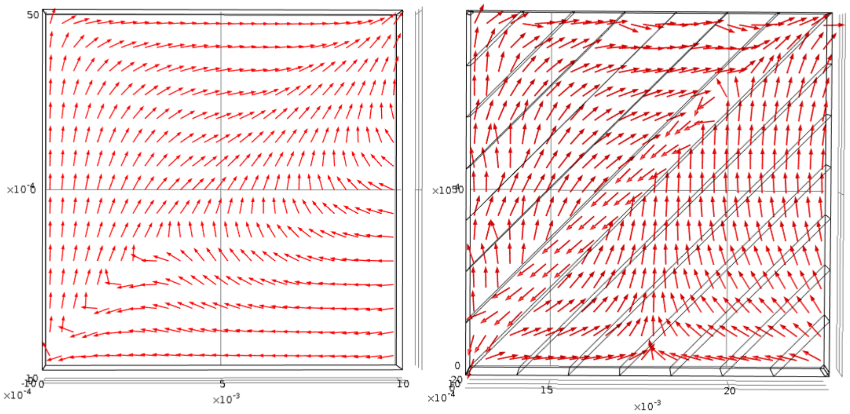

Figure 4.6: ASM (left) and ILM (right) shown with normalized eddy current density for open circuit Seebeck potential at 45 degree angle of inclination, aspect ratio of 1/1, and ten degree temperature difference top to bottom.

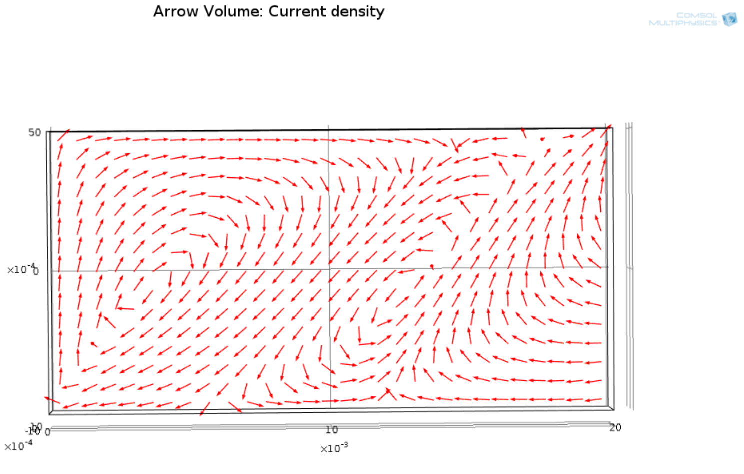

Figure 4.7: ASM normalized eddy current density for open circuit Seebeck potential at 45 degree angle of inclination, aspect ratio of 2/1, and ten degree temperature difference top to bottom.

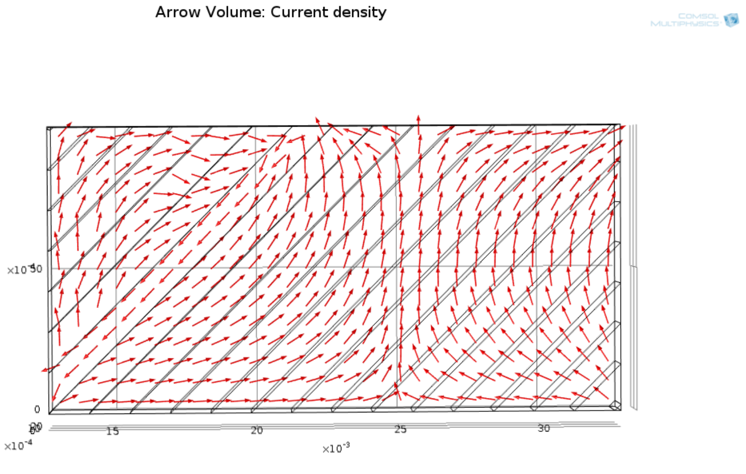

Figure 4.8: ILM normalized eddy current density for open circuit Seebeck potential at 45 degree angle of inclination, aspect ratio of 2/1, and ten degree temperature difference top to bottom.

4.1.5 Mathematical Difference in ILM and ASM

There is clearly a difference between eddy currents distributions in the ILM and ASM. The difference occurs in the application of Eq. 2.56. An examination of the eddy current equations with specific geometrical considerations from the transverse thermoelectric device described in section 2.2.2 provide the mathematical footing needed to understand thermoelectric eddy currents. Indicial notation comes in handy in for compact notation.

$$\nabla \times \mathbf{E} = -\frac{\partial \mathbf{B}}{\partial t} \tag{4.13}$$

$$(\nabla \times \mathbf{E})_i = \epsilon_{ijk}\partial_j E_k \tag{4.14}$$

$$\epsilon_{ijk}\partial_j E_k = 0 \tag{4.15}$$

Using Eqs. 2.48-2.53 and substituting them in Eq. 4.15, and breaking the cross product into components gives:

x component

$$(\nabla \times \mathbf{E})_x = \epsilon_{xjk}\partial_j E_k \tag{4.16}$$

$$(\nabla \times \mathbf{E})_x = \partial_y E_z - \partial_z E_y \tag{4.17}$$

$$0 = \frac{\partial}{\partial y}\left(\rho_{zx}J_x + \rho_{zz}J_z - S_{zx}\frac{\partial T}{\partial x} - S_{zz}\frac{\partial T}{\partial z}\right) - \frac{\partial}{\partial z}\left(\rho_{yy}J_y\right) \tag{4.18}$$

y component

$$(\nabla \times \mathbf{E})_y = \epsilon_{yjk}\partial_j E_k \tag{4.19}$$

$$(\nabla \times \mathbf{E})_y = \partial_z E_x - \partial_x E_z \tag{4.20}$$

$$\begin{aligned} 0 = \frac{\partial}{\partial z}\left(\rho_{xx}J_x + \rho_{xz}J_z\right) - \frac{\partial}{\partial z}\left(S_{xx}\frac{\partial T}{\partial x} + S_{xz}\frac{\partial T}{\partial z}\right) \\ - \frac{\partial}{\partial x}\left(\rho_{zx}J_x + \rho_{zz}J_z - S_{zx}\frac{\partial T}{\partial x} - S_{zz}\frac{\partial T}{\partial z}\right) \end{aligned} \tag{4.21}$$

z component

$$(\nabla \times \mathbf{E})_z = \epsilon_{zjk}\partial_j E_k \tag{4.22}$$

$$(\nabla \times \mathbf{E})_z = \partial_x E_y - \partial_y E_x \tag{4.23}$$

$$0 = \frac{\partial}{\partial x}\left(\rho_{yy}J_y\right) - \frac{\partial}{\partial y}\left(\rho_{xx}J_x + \rho_{xz}J_z - S_{xx}\frac{\partial T}{\partial x} - S_{xz}\frac{\partial T}{\partial z}\right) \tag{4.24}$$

Equations 4.18, 4.21, and 4.24 describe eddy currents in an anisotropic material. $J_y \neq 0$, but it is six orders of magnitude less than J_x and J_z as computed in the models and can be neglected. There is no y dependence for any of the variables, so the $\hat{x}$ and $\hat{z}$ components tell nothing about the system.

Eddy Currents in the ASM

The ASM is a pure mathematical model, and, hence, has certain idealistic assumptions that are not present in the ILM. The material parameters are broken into perpendicular and parallel components that are continuous throughout the anisotropic slab. Consequently, the material parameters are constants and are not spatially dependent. Examining the $\hat{y}$ component left from the curl of $\mathbf{E}$

$$\frac{\partial}{\partial z}\left(\rho_{xx}J_x+\rho_{xz}J_z-S_{xx}\frac{\partial T}{\partial x}-S_{xz}\frac{\partial T}{\partial z}\right)=\frac{\partial}{\partial x}\left(\rho_{zx}J_x+\rho_{zz}J_z-S_{zx}\frac{\partial T}{\partial x}-S_{zz}\frac{\partial T}{\partial z}\right) \tag{4.25}$$

Looking at the left hand side

$$\frac{\partial}{\partial z}\left(\rho_{xx}J_x+\rho_{xz}J_z-S_{xx}\frac{\partial T}{\partial x}-S_{xz}\frac{\partial T}{\partial z}\right) \tag{4.26}$$

$$\rho_{xx}\frac{\partial J_x}{\partial z}+\rho_{xz}\frac{\partial J_z}{\partial z}-S_{xx}\frac{\partial^2 T}{\partial z\partial x}-S_{xz}\frac{\partial^2 T}{\partial z^2}, \tag{4.27}$$

and then the right hand side

$$\frac{\partial}{\partial x}\left(\rho_{zx}J_x+\rho_{zz}J_z-S_{zx}\frac{\partial T}{\partial x}-S_{zz}\frac{\partial T}{\partial z}\right) \tag{4.28}$$

$$\rho_{zx}\frac{\partial J_x}{\partial x}+\rho_{zz}\frac{\partial J_z}{\partial x}-S_{zx}\frac{\partial^2 T}{\partial x^2}-S_{zz}\frac{\partial^2 T}{\partial x\partial z}. \tag{4.29}$$

Now, $\rho_{xz}=\rho_{zx}$ and $S_{xz}=S_{zx}$. Bringing the pieces back together and simplifying gives

$$\begin{aligned}\rho_{xx}\frac{\partial J_x}{\partial z}+\rho_{xz}\left(\frac{\partial J_z}{\partial z}-\frac{\partial J_x}{\partial x}\right)-\rho_{zz}\frac{\partial J_z}{\partial x}&\\ =S_{xz}\left(\frac{\partial^2 T}{\partial z^2}-\frac{\partial^2 T}{\partial x^2}\right)+S_{xx}\frac{\partial^2 T}{\partial z\partial x}-S_{zz}\frac{\partial^2 T}{\partial x\partial z}.&\end{aligned} \tag{4.30}$$

Eddy Currents in the ILM

The situation gets more complicated in the ILM since the coefficients are spatially dependent over each layer of alternating materials. The product rule must be used for each term in the sums. Again looking at the y component. The left hand side says

$$\frac{\partial}{\partial z}\left(\rho_{xx}J_x + \rho_{xz}J_z - S_{xx}\frac{\partial T}{\partial x} - S_{xz}\frac{\partial T}{\partial z}\right) \tag{4.31}$$

$$\begin{aligned}\frac{\partial \rho_{xx}}{\partial z}J_x + \rho_{xx}\frac{\partial J_x}{\partial z} + \frac{\partial \rho_{xz}}{\partial z}J_z + \rho_{xz}\frac{\partial J_z}{\partial z}& \\ - \frac{\partial S_{xx}}{\partial z}\frac{\partial T}{\partial x} - S_{xx}\frac{\partial^2 T}{\partial z \partial x} - \frac{\partial S_{xz}}{\partial z}\frac{\partial T}{\partial z} - S_{xz}\frac{\partial^2 T}{\partial z^2}&,\end{aligned} \tag{4.32}$$

and then the right hand side

$$\frac{\partial}{\partial x}\left(\rho_{zx}J_x + \rho_{zz}J_z - S_{zx}\frac{\partial T}{\partial x} - S_{zz}\frac{\partial T}{\partial z}\right) \tag{4.33}$$

$$\begin{aligned}\frac{\partial \rho_{zx}}{\partial x}J_x + \rho_{zx}\frac{\partial J_x}{\partial x} + \frac{\partial \rho_{zz}}{\partial x}J_z + \rho_{zz}\frac{\partial J_z}{\partial x}& \\ - \frac{\partial S_{zx}}{\partial x}\frac{\partial T}{\partial x} - S_{zx}\frac{\partial^2 T}{\partial x^2} - \frac{\partial S_{zz}}{\partial x}\frac{\partial T}{\partial z} - S_{zz}\frac{\partial^2 T}{\partial x \partial z}&.\end{aligned} \tag{4.34}$$

Then again putting the pieces back together

$$\begin{aligned}
&\rho_{xx}\frac{\partial J_x}{\partial z} + \rho_{xz}\left(\frac{\partial J_z}{\partial z} - \frac{\partial J_x}{\partial x}\right) - \rho_{zz}\frac{\partial J_z}{\partial x} + \left(\frac{\partial \rho_{xx}}{\partial z} - \frac{\partial \rho_{zx}}{\partial x}\right) J_x + \left(\frac{\partial \rho_{xz}}{\partial z} - \frac{\partial \rho_{zz}}{\partial x}\right) J_z \\
&= S_{xz}\left(\frac{\partial^2 T}{\partial z^2} - \frac{\partial^2 T}{\partial x^2}\right) + S_{xx}\frac{\partial^2 T}{\partial z \partial x} - S_{zz}\frac{\partial^2 T}{\partial x \partial z} - \left(\frac{\partial S_{zx}}{\partial x} - \frac{\partial S_{xx}}{\partial z}\right)\frac{\partial T}{\partial x} \\
&\qquad - \left(\frac{\partial S_{zz}}{\partial x} - \frac{\partial S_{xz}}{\partial z}\right)\frac{\partial T}{\partial z}
\end{aligned} \tag{4.35}$$

The situation becomes more complicated in the ILM as seen by comparing Eq. 4.30 and Eq. 4.35. There are 8 more terms in $(\nabla \times \mathbf{E})_y$ equation in the ILM than the ASM. The results are seen by the more complicated current density directions in the ILM in Figs. 4.5, 4.6, 4.7, and 4.8.

Effect of Width

In the description of transverse thermoelectric effects in the previous chapter only two dimensions were discussed. The reason is that the third dimension is of no consequence, but this statement definitely needs to be qualified. So simulations were run with a varying third dimension to demonstrate that there is no variation in the y-direction.

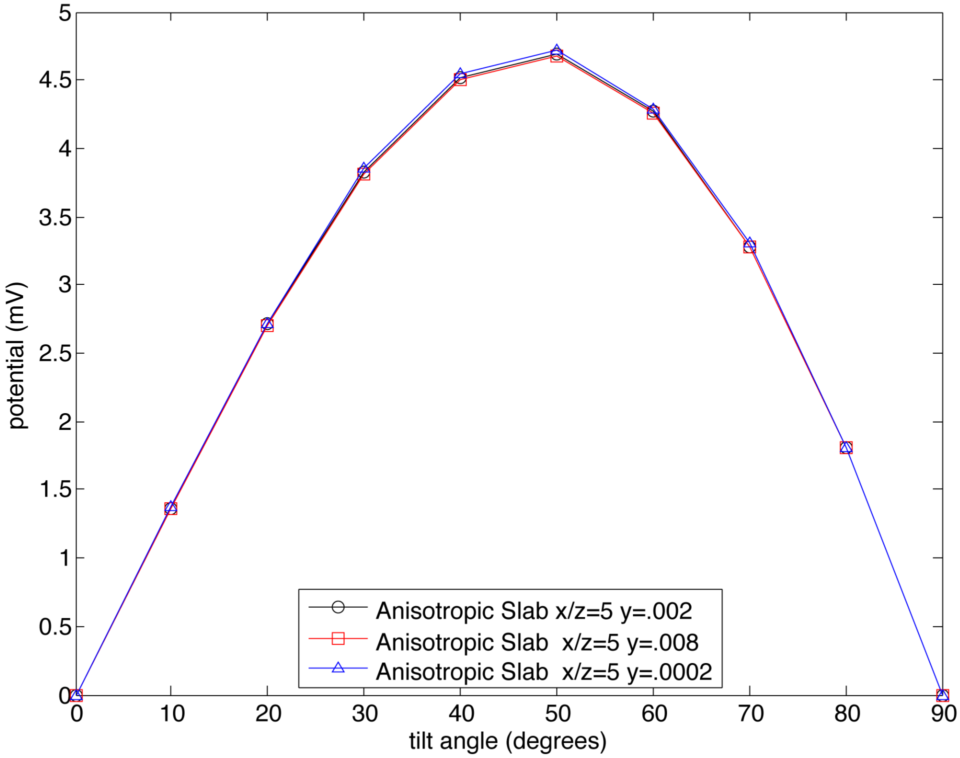

Figure 4.9: Effect of width on the ASM for angles of inclination 0°-90°.

The Seebeck study provided some interesting results. Eddy currents occur and must be taken into account when running simulations to compute thermopower. The dimension of the device determine which angle of inclination should be used for maximum thermopower output. The thermoelectric effect is a thermodynamically reversible process, and the computational study of the Peltier effect is presented next.

4.2 Transverse Peltier Effect

In this study an electrical current boundary condition was input to model the Peltier effect. The angle of inclination was kept at 25°, and the bottom surface was held at $295K$ as in the Kyarad experiment. Different current densities were input for different aspect ratios. Both models have a temperature gradient along the top of the device where the cooling occurs. The temperature was taken in the middle of the top surface as this location was shown to be in close agreement with the surface average. Bismuth telluride and lead were the materials used for the study. The materials' parameters used are the same as found in Table 1 in Kyarad [6] with the exception that a Seebeck coefficient of $200(\mu V/K)$ was used instead of $20(\mu V/K)$.

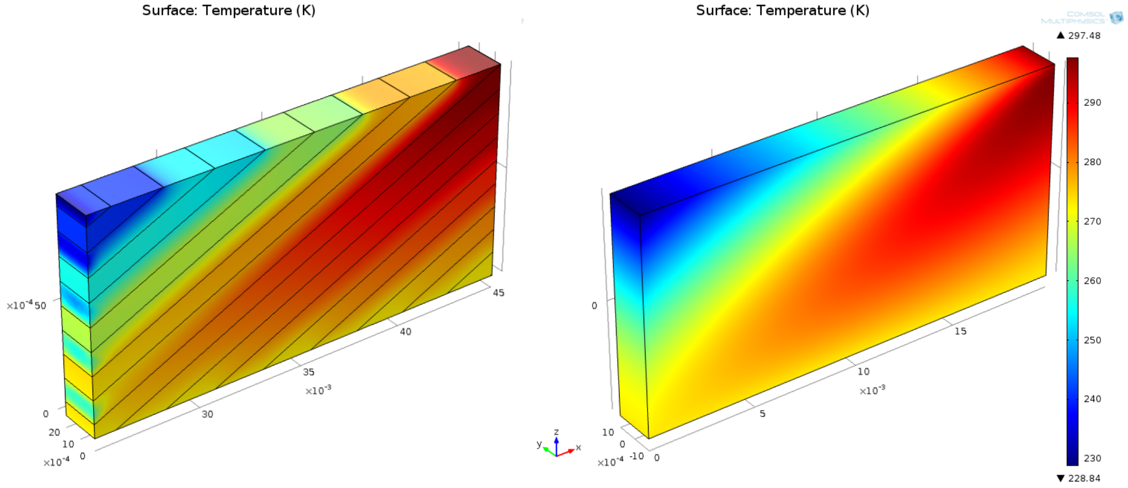

Figure 4.10: Temperature distribution across thermoelectric device CAD model of Peltier effect for ILM and ASM.

4.2.1 Peltier Aspect Ratio Comparison

While in the Seebeck study the ASM and ILM agreed extremely well over different geometries and conditions, the Peltier simulations diverged for certain device geometries. In the Peltier studies Fig. 4.11, the ILM diverged significantly at lower aspect ratios with the layer thickness of 1mm used in the Kyarad experiment [6]. This includes the aspect ratio used in [6]. At the aspect ratio of 5 the models converge, and the results for longer aspect ratios are discussed next.

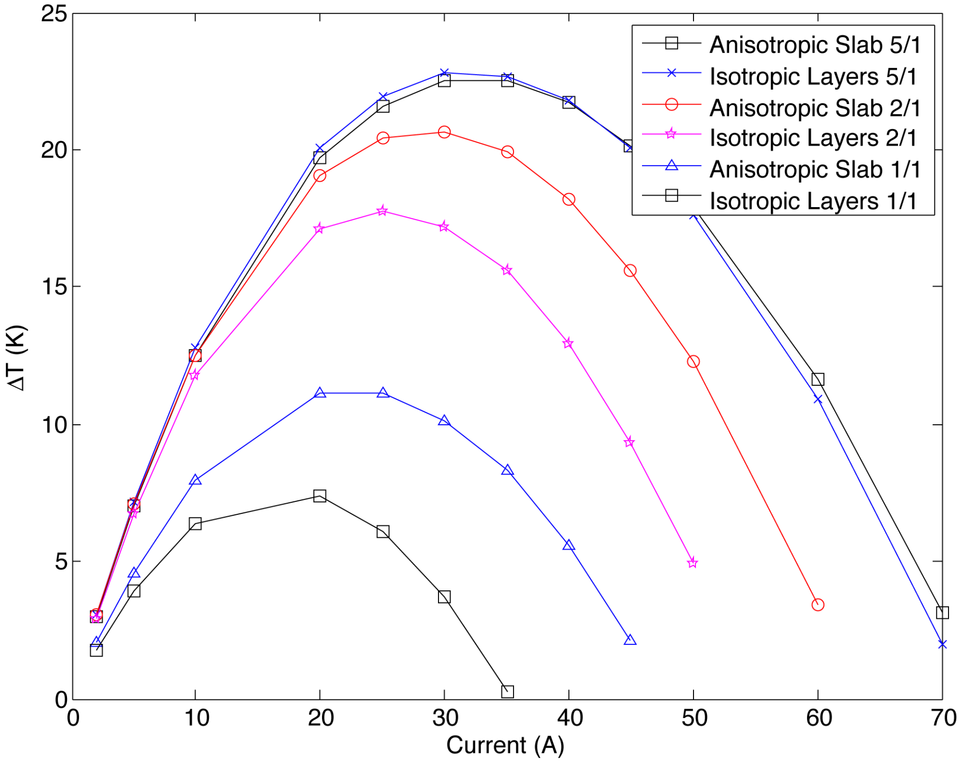

Figure 4.11: Temperature difference created in z-direction for injected currents for ILM and ASM for aspect ratios $\Delta x/\Delta z$ =(5,2,1).

Further exploration shows that the models diverge again at higher aspect ratios.

In Fig. 4.12 the ILM shows a small decrease in ΔT for aspect ratio $\Delta x/\Delta z = 10$. This implies an engineering limit in geometry for Peltier coolers as for longer devices Joule heating will start to overtake the Peltier cooling. Keeping the cross sectional area the same as in done in the studies, this makes sense looking at the equation for Joule heating

$$Q \propto I^2 R \;=\; I^2 \rho \left(\frac{L}{A}\right). \tag{4.36}$$

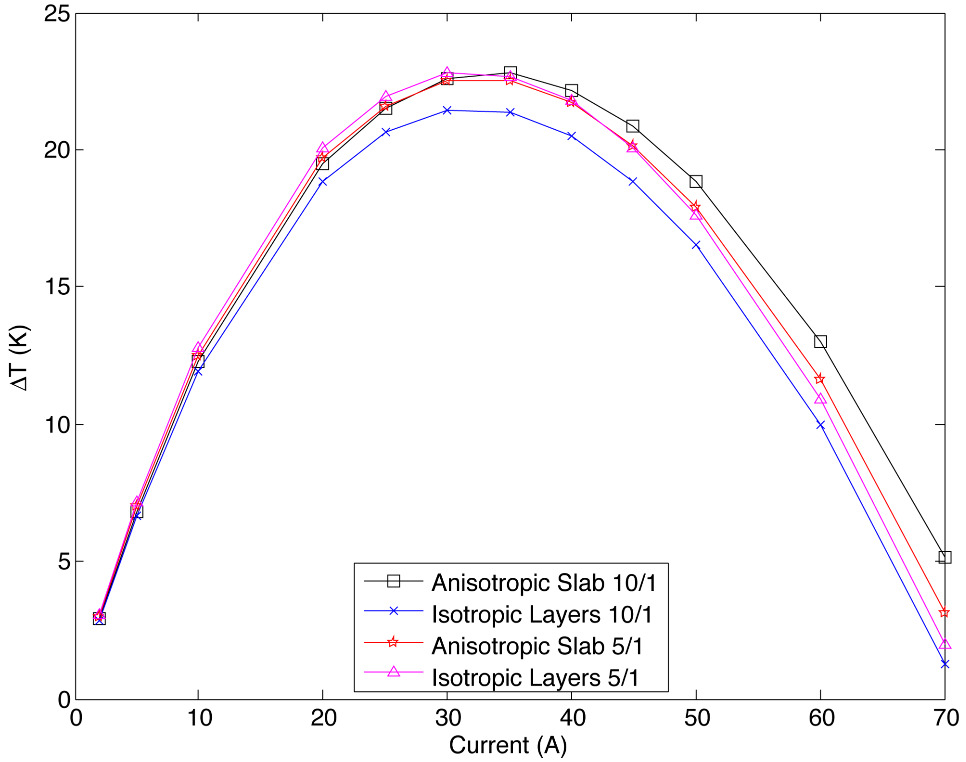

Figure 4.12: Temperature difference for aspect ratio $\Delta x/\Delta z = (10, 5)$ showing the divergence of models at high aspect ratio.

Peltier Model Convergence: Layer Thickness

The ILM converges to the ASM when the layer thickness was reduced as shown in Fig. 4.13. This is a comforting result in the limit, however it may be a drawback of the ILM in general as it diverges significantly from measured data.

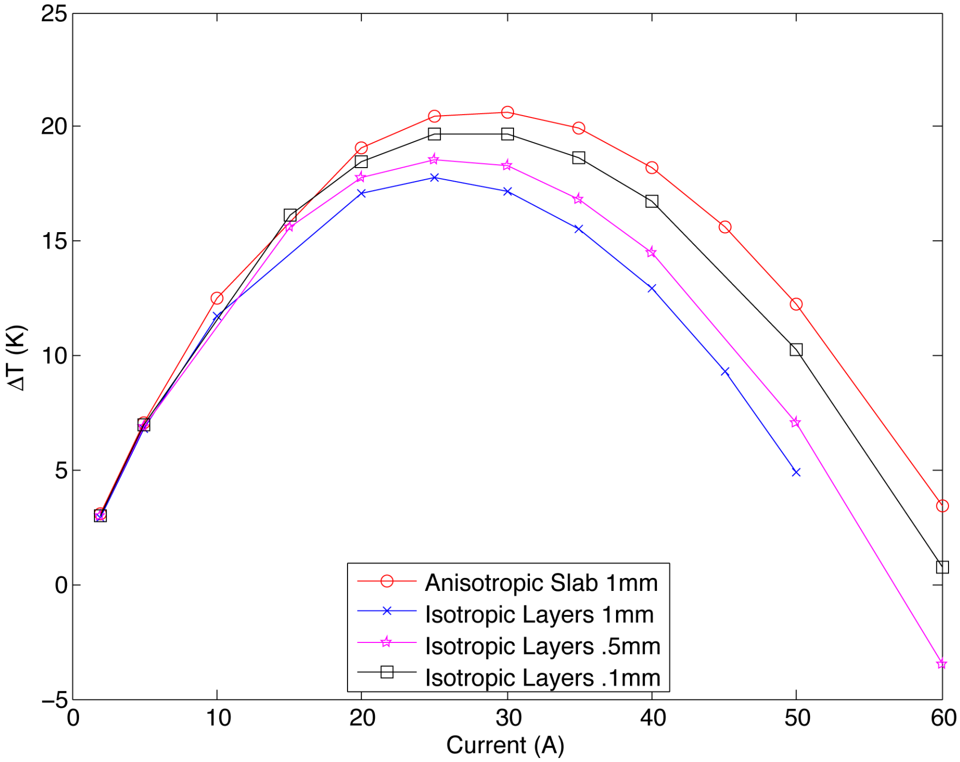

Figure 4.13: Convergence of ILM to ASM in the limit that layer thickness goes to zero $t_A \to 0$ and $t_B \to 0$.

4.2.2 ASM and ILM Differences

Temperature Distribution

As noted for the potential in the Seebeck studies, there is a similar difference in distribution of temperature in the Peltier studies. Again the ILM has a digital effect from the inhomogeneity of the alternating material properties of each layer. In the ILM the temperature is constant across most of each layer, and temperature drops only occur at the interfaces of the two materials. This is a comforting result since the Peltier is known to occur at material interfaces. The strict mathematical model employed in the ASM has the smooth profile shown in Fig. 4.14. As noted in the previous section, the temperature difference ΔT is greater in the ASM. This is an important difference of the ILM. More comparisons to measured data are needed to determine if this is a drawback if the ILM or if the ILM is a more realistic model.

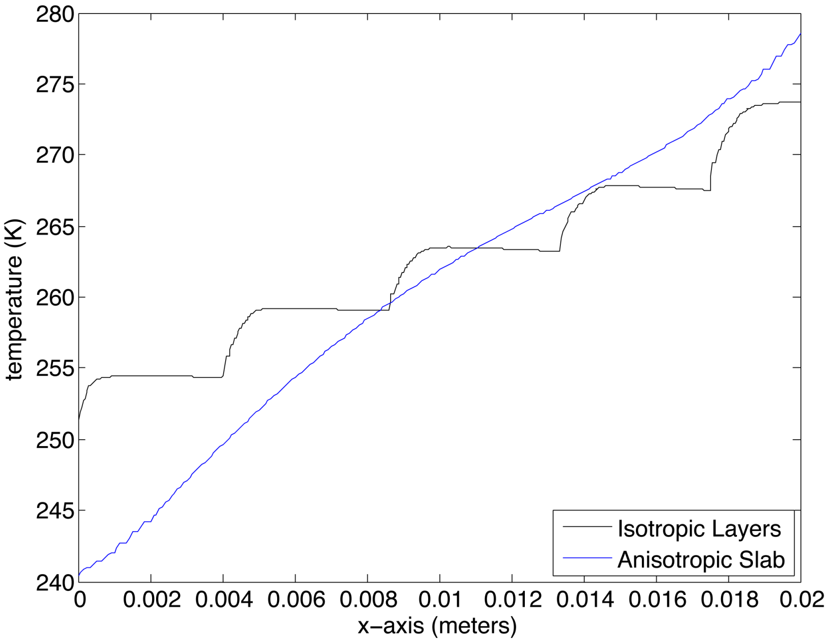

Figure 4.14: Difference in temperature distribution across x-direction for the ASM and ILM in a Peltier effect simulation.

Current Density Differences

A current density plot Fig. 4.15 show an important difference in the two computational models. There is a component in the ILM that does not show up in the ASM. An input current in the x-direction mandates that a z directed electric field component is generated as indicated in Eq. 4.37.

$$E_z = J_x \rho_{zx} + J_z \rho_{zz} - S_{zx} \left(\frac{\partial T}{\partial x} \right) - S_{zz} \left(\frac{\partial T}{\partial z} \right) \tag{4.37}$$

Indeed the z component of the current density is seen in Fig. 4.15 is seen in both models. However, there is an important difference in the ILM and ASM that must be accounted for in the engineering of thermoelectric devices.

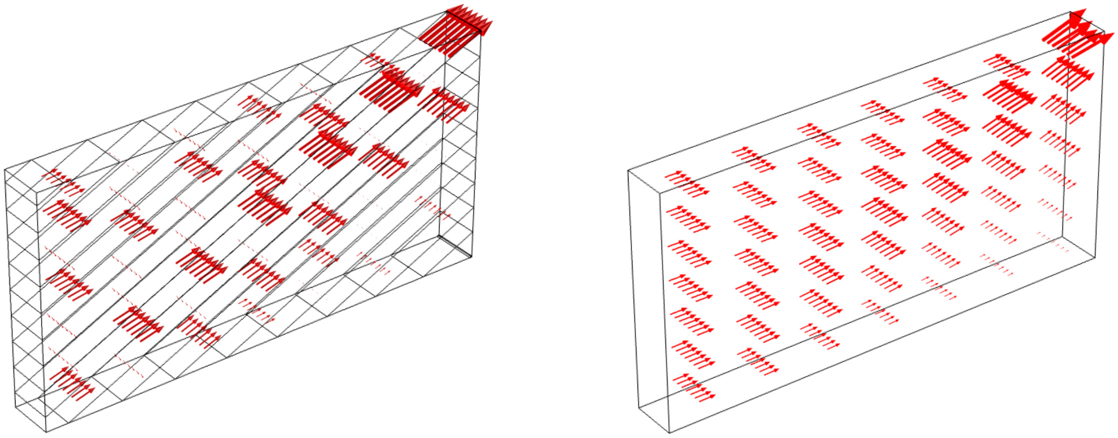

Figure 4.15: Current density plots for ILM and ASM showing the extra component in the ILM.

Zooming in for a closer look at Fig. 4.16 and Fig. 4.17 reveals a component perpendicular to the contact surfaces in the ILM not seen in the ASM. This $J_\perp$ at a surface interface is directed by an $E_\perp$ as described in the paper by Anatychuk and Luste [10]. $E_\perp$ occurs throughout the model in all the Peltier effect simulations using the ILM. $E_\perp$ only occurs in "zonally inhomogeneous structures" [10] with the materials posessing different Seebeck coefficients. Moreover Anatychuk and Luste state that the $E_\perp$ fields lie along isotherms within the material. Utilizing the plotting capabilities in COMSOL, it looks as though they are correct as there are isothermal surfaces that intersect the contact surfaces perpendicularly. E_z is positive as seen in both the ASM and ILM, however the z component of $E_\perp$ is in the negative z direction. Therefore, $E_\perp$ is subtracting from the overall heat transfer in the Peltier cooling.

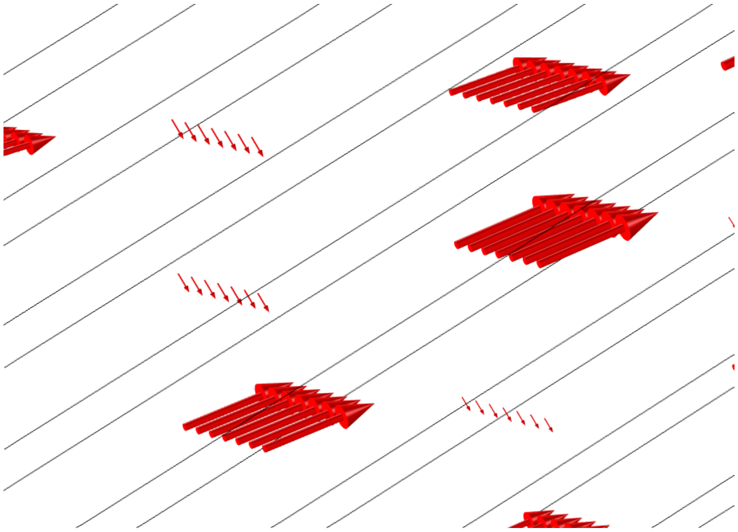

Figure 4.16: Zoomed in current density plot for the Peltier ILM simulation showing extra surface perpendicular component.

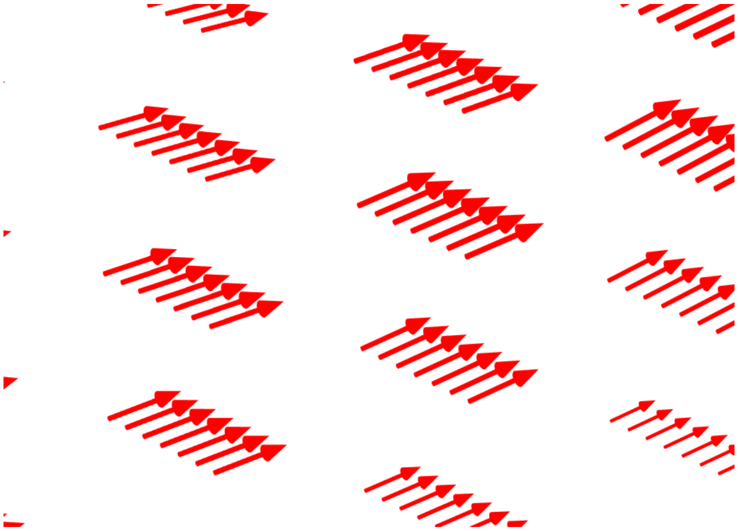

Figure 4.17: Zoomed in current density plot of Peltier ASM simulation showing no surface perpendicular component.

4.3 Device Engineering

4.3.1 ILM

Pictured below in Fig. 4.18 is a device with dimensions of 5cm x 5mm x 5mm. The top and bottom plates are beryllium oxide, and the left and right plates are copper. The materials in the middle alternate between lead and p-type bismuth telluride.

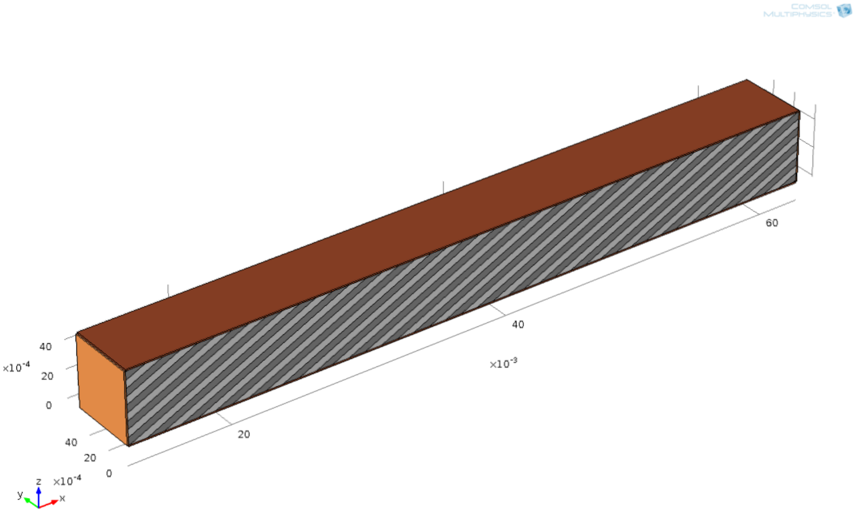

Figure 4.18: Single transverse thermoelectric device geometry built in the ILM.

Fig. 4.19 shows the potential distribution over a transverse thermoelectric device with heat flux applied of $137,000 (W/m^2)$ to top, and $0V$ held at right side. The choice of $137,000 (W/m^2)$ for the input heat flux simulates a magnification of 100 times that of sunlight which has a heat flux of $1370 (W/m^2)$. The bottom surface is held at a constant temperature of 295K which assumes perfect heat flux to create the heat sink.

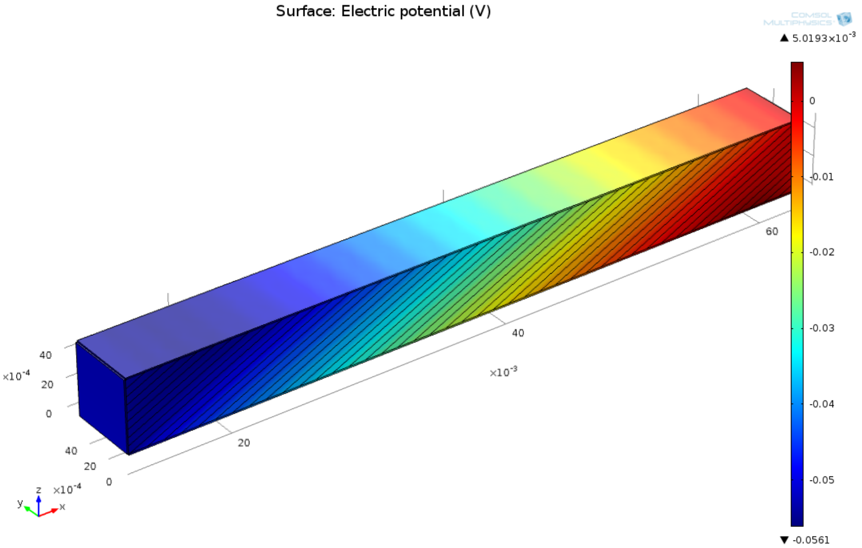

Figure 4.19: ILM surface plot of the potential distribution over a transverse thermoelectric device with heat flux applied of $137,000 (W/m^2)$ to top, and $0V$ held at right side.

4.3.2 ASM

The ILM geometries are more realistic than the ASM, so the ILM CAD device geometries are more complicated. Consequently, creating devices for the ILM takes much longer than creating devices in the ASM. It is possible to create geometries in other CAD programs and import them into COMSOL which could simplify the process of creating complicated geometries in the ILM. Although the ASM is an idealization, building a model a large set up for a device takes much less time. The ASM Fig. 4.20 plots the potential across the mathematical model of the ILM device in Fig. 4.19.

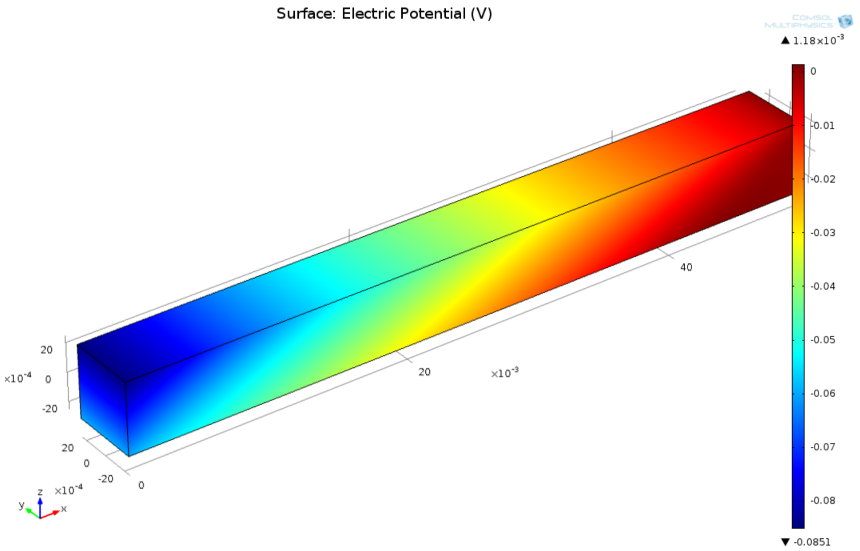

Figure 4.20: ASM model of a single transverse thermoelectric with heat flux applied of $137,000 (W/m^2)$ to the top section, and $0V$ held at bottom right side copper plate.

Fig. 4.21 pictures an array of single devices electrically linked in series with copper plates. Each leg is made of the same two types of materials, so unlike longitudinal thermoelectric devices, only one type of thermoelectric semiconductor is needed to build a device. The important aspect that needs to be considered is the orientation of each thermoelectric leg. Each leg must be oriented 180° relative to the next. This is must be the case if the voltages are to add in series rather than simply cancel each other out. This being the case, the potentials add in series. The potential is higher in the ASM Fig. 4.20 than in the ILM Fig. 4.19, and these differences need to be more thoroughly examined. Regardless of the differences, the ASM can be used to get an upper bound on device output. The ASM physics module needs to be generalized somewhat in order to achieve an effective simulation. The more robust ASM will be able to input alternating angles of orientation such that this effect can be effectively modeled in more complicated devices.

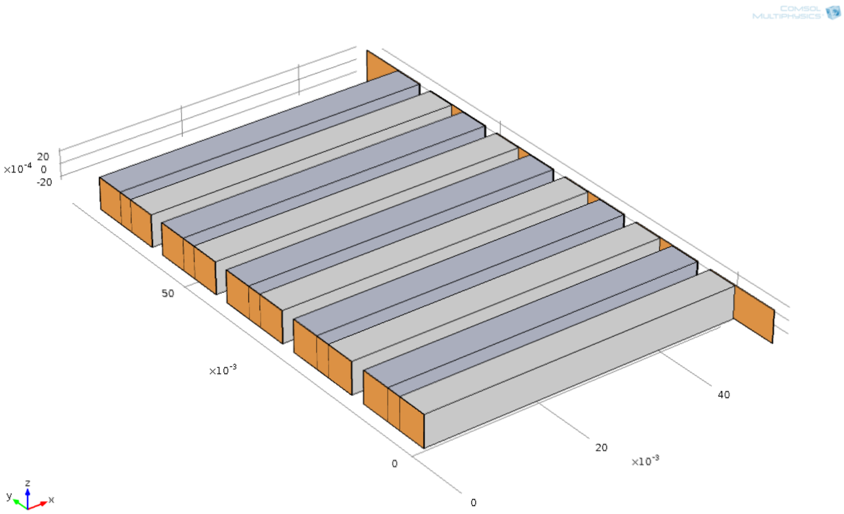

Figure 4.21: Transverse thermoelectric device linked in series with heat flux applied of $137,000(W/m^2)$ to the top of each section, and $0V$ held at bottom right side copper plate.

This section provides the evidence that transverse thermoelectric devices can be modeled and engineered in a computational environment in COMSOL. Further device geometries and environmental conditions can be input in order to compare outputs before spending the time and money creating physical devices and taking measurements.

The transverse Seebeck and Peltier effects have been shown to be effective. Open circuit eddy currents and surface interface electric fields have proven to be interesting effects that must be taken into account to understand transverse thermoelectrics. More studies are needed to determine the necessary materials and conditions needed to engineer optimal devices.

Chapter 5

Conclusion

COMSOL Multiphysics uses the finite element method (FEM) to compute numerical solutions and was the main software used in the analysis of the transverse thermoelectric effect done for this thesis. As COMSOL does not have a thermoelectric module, two COMSOL physics modules were built for modeling and research. The purely mathematical model named the anisotropic slab model (ASM) provides the ideal case with which to compare the isotropic layer model (ILM). The ILM provides the more realistic model as the geometries and boundary conditions match what an actual device will encounter. The differences in ILM FEM solutions are noted throughout the thesis and provide computational evidence as to predicted effects such as anisotropic eddy currents and surface to surface interface effects. Validation with measured data along with the computational evidence for the aforementioned effects prove the reliability of the custom physics modules.

The transverse Seebeck potential was shown to add in series for longer devices.

Noted also was that although no current was injected into the device, eddy currents are generated and have a significant effect on the output potential that cannot be neglected. The angular dependence on output was shown to originate from the competition of the longitudinal Seebeck element S_{xx} and the off diagonal element S_{xz} of the Seebeck tensor. The third dimension has no effect on the output and, hence, does not need to be considered for loss mechanisms. Transverse Seebeck effect is shown to be a reliable mechanism for thermoelectric device engineering.

The transverse Peltier effect was shown to have a cooling effect of approximately $20K$. In the ILM portions of the current were directed perpendicularly to the layers' interfaces through out the device. This perpendicular component was absent in the ASM since it is an idealization without layer to layer interfaces. As seen in the simulations, when the layer thickness is reduced the ILM converges to the ASM. This is a deficiency in the ILM since certain device geometries might have comparable layer thickness relative to the dimensions of the device. Temperature drops in the ILM were shown to occur at the interface of the layers while the ASM was shown to have a continuous drop. The transverse Peltier effect exhibits possibilities for applications such as computer chip cooling.

Transverse thermoelectric devices have promising future in energy conversion and heat transfer. At a cost of approximately $10,000 per pound to carry a load into space, reduction in material to power spacecrafts opens up a valuable margin which can be utilized for more computational power or simply less cost. In any process which produces heat loss, transverse thermoelectric devices could be could be used to convert the loss into electrical power supplied back into the grid. Solar power conversion is yet another application that should drive research and development transverse thermoelectric devices.

Appendix A

Landauer Approach

A.1 Charge Current

There are two ways that an electrical current is generated in a thermoelectric device. To generate a current there must be a difference in Fermi distributions such that an equilibrium will be reached in a steady state. One method is to apply voltage, and another is to apply a temperature gradient across the device. This derivation follows the one energy model given in Lundstrom's course [18].

If the two contacts are held at the same temperature, so that $\Delta T = 0$, current will flow if we apply a small voltage such that $\Delta E_F \neq 0$. Fig. A.1 [18] illustrates this concept.

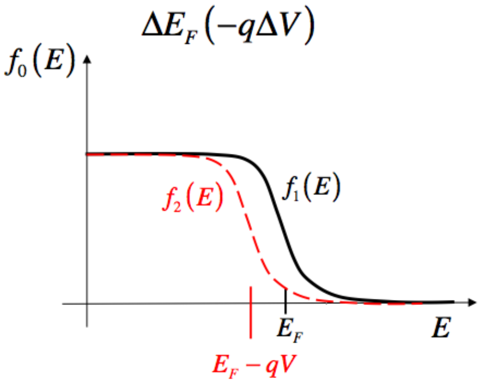

Figure A.1: A change in Fermi distribution due to an applied potential

$$(f_1 - f_2) \approx \left(-\frac{\partial f_0}{\partial E}\right) q\Delta V \tag{A.1}$$

When temperature is the driving generalized force behind the current and no applied voltage, we have $\Delta T \neq 0$ and $\Delta E_F = 0$. Fig. A.2 [18] shows this change.

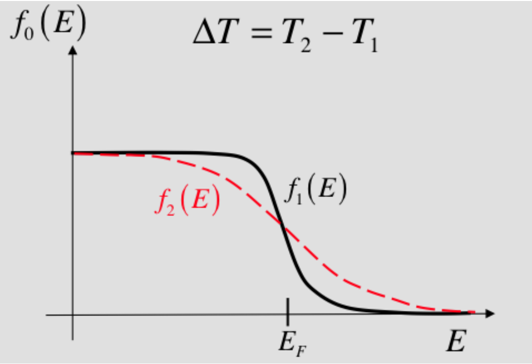

Figure A.2: A change in Fermi distribution due to a change in temperature.

Expanding f_2 in a Taylor series we have:

$$(f_1 - f_2) \approx f_1 - (f_1 + \frac{\partial f_1}{\partial T}\Delta T) \tag{A.2a}$$

$$\approx -\frac{\partial f_1}{\partial T}\Delta T \tag{A.2b}$$

Differentiating f_1 with respect to T we have

$$\frac{\partial f_1}{\partial T} = -\frac{(E - E_F)}{T}\left(\frac{\partial f_0}{\partial E}\right) \tag{A.3}$$

So, for a temperature gradient

$$(f_1 - f_2) \approx -\left(-\frac{\partial f_0}{\partial E}\right)\frac{(E - E_F)}{T}\Delta T \tag{A.4}$$

Now, if there is a temperature gradient as well as a difference in Fermi levels as shown in Fig. A.3 [18], then the contributions add to get

$$(f_1 - f_2) \approx \left(-\frac{\partial f_0}{\partial E}\right) q\Delta V - \left(-\frac{\partial f_0}{\partial E}\right)\frac{(E - E_F)}{T}\Delta T \tag{A.5}$$

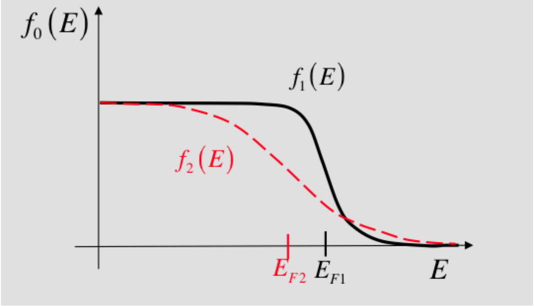

Figure A.3: A change in Fermi distribution due to a change in temperature and an applied voltage.

The equation for current is

$$I(E_0) = \frac{2q}{h} T(E_0) M(E_0)(f_1 - f_2) \tag{A.6}$$

Plugging in Eq. A.5 into Eq. A.6,

$$I(E_0) = \frac{2q}{h} T(E_0) M(E_0) \left\{ \left(-\frac{\partial f_0}{\partial E}\right) q\Delta V - \left(-\frac{\partial f_0}{\partial E}\right) \frac{(E - E_F)}{T} \Delta T \right\} \tag{A.7}$$

$$I(E_0) = G(E_0)\Delta V - [SG(E_0)]\,\Delta T \tag{A.8}$$

where,

$$G(E_0) = \frac{2q^2}{h} T(E_0) M(E_0) \left(-\frac{\partial f_0}{\partial E}\right) \tag{A.9}$$

$$SG(E_0) = \frac{2q}{h} T(E_0) M(E_0) \left(-\frac{\partial f_0}{\partial E}\right) \frac{(E_0 - E_F)}{T} \tag{A.10}$$

$$S(E_0) = -\left(\frac{k_B}{q}\right) \frac{(E_0 - E_F)}{k_B T} \tag{A.11}$$

A.2 Heat Current

Electrons certainly carry charge, but they also carry heat. Thermodynamically the system must come to thermal equilibrium, so electrons are driven by an entropic force to distribute the energy in the system. A similar approach that was used in the previous section to derive the electrical current equation provides a way to calculate heat flux.

$$I_{Q_1}(E_0) = \frac{2(E_0 - E_{F1})}{h} T(E_0) M(E_0)(f_1 - f_2) \tag{A.12}$$

$$I_{Q_2}(E_0) = \frac{2(E_0 - E_{F2})}{h} T(E_0) M(E_0)(f_1 - f_2) \tag{A.13}$$

Near equilibrium the heat flux is almost at a steady state and $f_1 \approx f_2 \approx f_0$, so

$$I_{Q_1} \approx I_{Q_2} \rightarrow I_Q(E_0) = \frac{2(E_0 - E_F)}{h} T(E_0) M(E_0)(f_1 - f_2) \tag{A.14}$$

Starting with the form we have for $(f_1 - f_2)$ and using Eq. A.10

$$(f_1 - f_2) \approx C_1(E_0) q \Delta V + C_2(E_0) \Delta T \tag{A.15}$$

$$I_Q(E_0) = \frac{2}{h} T(E_0) M(E_0) \left((E_0 - E_F) q \Delta V - \frac{(E_0 - E_F)^2}{T} \Delta T \right) \tag{A.16}$$

$$I_Q(E_0) = T \left[S G(E_0) \right] \Delta V - K_0(E_0) \Delta T \tag{A.17}$$

where

$$K(E_0) = \frac{2}{h}\frac{(E_0 - E_F)^2}{T}T(E_0)M(E_0)\frac{\partial f_0}{\partial E}. \tag{A.18}$$

We now have equations for both heat and electric current. This set of equations is called the coupled current equations, and they describe how heat and current flow in materials.

$$I_Q(E_0) = T\left[SG(E_0)\right]\Delta V - K_0(E_0)\Delta T \tag{A.19}$$

$$I(E_0) = G(E_0)\Delta V - \left[SG(E_0)\right]\nabla T \tag{A.20}$$

Appendix B

Computation Tables

B.1 Zahner et al. Validation Tables

ILM 3/17/2014

For $q_{in} = 10(mW/cm^2)$, slice thickness=0.1mm, ΔT values added to T_{bottom} 275.13K, the bottom temperature. Reference: [16]

α	15	20	25	30	35	40	45	50	60
U(μV)	.143	.178	.192	.192	.187	.178	.166	.142	.111
ΔT(mK)	4.45	3.95	3.49	3.01	2.62	2.26	1.97	1.72	1.37

Table B.1: Computations of ILM for the Zahner confirmation simulations to determine the validity of the custom physics modules.

ASM 2/21/2014

For $q_{in} = 10(mW/cm^2)$, slice thickness=0.1mm, ΔT values added to T_{bottom} 275.13K, the bottom temperature. Reference: [16]

α	0	10	15	25	35	45	55	65	75
U(μV)	1.73e-4	.105	.147	.192	.192	.166	.130	.092	7.31e-2
ΔT(mK)	5.25	4.88	4.48	3.5	2.61	1.95	1.49	1.20	1.11

Table B.2: Computations of ASM for the Zahner confirmation simulations to determine the validity of the custom physics modules.

B.2 Kyarad et al. Validation Tables

ASM 2/25/2014

For x=0.02m, z=0.01m, y=0.002m, α=25°, p=1, T_{bottom}=295K. Reference: [6].

I_{in}(A)	T_{min}(K)	$T_{midpoint}$(K)	$T_{surfAvg}$(K)
1	292.33	293.44	293.45
5	282.58	287.9	287.94
10	272.34	282.47	282.56
15	264.03	278.52	278.68
20	257.42	275.93	276.16
25	252.32	274.57	274.88
30	248.55	274.33	274.73
35	245.98	275.1	275.59
40	244.46	276.81	277.34
45	243.88	279.38	280.04
50	244.14	282.74	283.47
55	245.15	286.83	287.63
60	246.84	291.59	292.46

Table B.3: Computations of ASM for the Kyarad confirmation simulations to determine the validity of the custom physics modules.

ILM 3/17/2014

For x=0.02m, z=0.01m, y=0.002m, α=25°, p=1, T_{bottom}=295K. No surface temperature computations. Reference: [6].

I_{in}(A)	J_{in}(A/m^2)(10^5)	$T_{midpoint}$(K)
2	1	292.71
4	2	290.55
10	5	284.84
20	10	277.74
30	15	273.39
40	20	271.49
50	25	271.8
60	30	274.1
70	35	278.18
80	40	283.87

Table B.4: Computations of ILM for the Kyarad confirmation simulations to determine the validity of the custom physics modules.

Appendix C

List of Symbols

Symbol	Definition	Units
p	momentum	$(kg \cdot m/s)$
p	layer thickness ratio (t_B t_A)	*none*
F	force	N
E_F	Fermi energy	eV
E_C	conduction band energy	eV
$E(p)$	kinetic energy	eV
F_n	quasi-Fermi energy	eV
τ_f	relaxation time	s
k_B	Boltzmann constant	$(m^2 \cdot kg)/(s^2 \cdot K)$
T	absolute temperature	K
v	velocity	m/s

$\mathcal{F}$	generalized force	
σ	electrical conductivity	S/m
G	electrical conductivity	S/m
ρ	electrical resistance	$Ohm \cdot m$
J	current density	A/m^2
J_Q	heat flux density	W/m^2
q	heat flux density	W/m^2
S	Seebeck coefficient	V/K
Q	joule heating	J
E	electric field	V/m
V	electric potential	V
K	thermal conductivity	$W/(m \cdot K)$
κ	thermal conductivity	$W/(m \cdot K)$
Π	Peltier coefficient	V
∇	differential operator	*none*
$S_{\parallel}$	parallel Seebeck coefficient	V/K
$S_{\perp}$	series Seebeck coefficient	V/K
$\sigma_{\parallel}$	parallel electrical conductivity	S/m
$\sigma_{\perp}$	series electrical conductivity	S/m

$\kappa_{\parallel}$	parallel thermal conductivity	$W/(m \cdot K)$
$\kappa_{\perp}$	series thermal conductivity	$W/(m \cdot K)$

Table C.1: Symbols used throughout the paper.

Bibliography

[1] www.britannica.com. Jean-charles-athanase peltier, 2014.

[2] http://www.thermoelectrics.caltech.edu/. Thomson effect, 2014.

[3] Jeff Snyder.

[4] NASA. Voyager: The interstellar mission, 2013.

[5] Mark Lundstrom. *Fundamentals of Carrier Transport*. Cambridge University Press, 2009.

[6] A. Kyarad and H. Lengfellner. Transverse peltier effect in tilted pbbi2te3 multilayer structures. *Applied Physics Letters*, 89(19), 2006.

[7] C. Reitmaier, F. Walther, and H. Lengfellner. Transverse thermoelectric devices. *Applied Physics A: Materials Science and Processing*, 99(4):748 – 753, 2010.

[8] A. A. Snarskii, A. M. Pal'ti, and A. A. Ashcheulov. Anisotropic thermocouples article. *Fiz. Tekh. Poluprovodn*, 31:1281 – 1298, November 1997.

[9] L. I. Anatychuk and O. J. Luste. Thermoelectric eddy currents. calculation and

control methods. In *Thermoelectrics, 1997. Proceedings ICT '97. XVI International Conference on*, pages 595–598, Aug 1997.

[10] L. I. Anatychuk and O. Ya. Luste. Thermoelectric eddy currents and transverse thermal emf in zonally in homogeneous plates. *The Soviet Physics Journal*, 12(6):801 – 803, 1969.

[11] A. G. Samoilovich and A. A. Snarskii. Investigation of thermoelectric eddy currents. *Fiz. Tekh. Poluprovodn*, 13:1539 – 1547, August 1979.

[12] L.I. Anatychuk. *Materials, Preparation, and Characterization in Thermoelectrics*. CRC Press, 2012.

[13] Roland W. Lewis, Permual Nithiarasu, and Kankanhalli N. Seetharamu. *Fundamentals of the Finite Element Method for Heat and Fluid Flow*. John Wiley and Sons, Ltd, 2004.

[14] COMSOL. *Physics Interface Builder User's Guide*, 2012.

[15] V.P. Babin, T.S. Gudkin, Z.M. Dashevskii, L.D. Dudkin, E.K. Iordanishvili, V.I. Kaidanov, N.V. Kolomoets, O.M. Narva, and L.S. Stilbans. Anisotropic synthetic thermoelements and their maximum capabilities. *Sov. Phys. Semicond.*, 8(4):748 – 753, 1974.

[16] Th. Zahner, R. Frg, and H. Lengfellner. Transverse thermoelectric response of a tilted metallic multilayer structure. *Applied Physics Letters*, 73(10):1364–1366, 1998.

[17] Syed Ashraf Ali and Sandip Mazumder. Computational study of transverse peltier coolers for low temperature applications. *International Journal of Heat and Mass Transfer*, 62(0):373 – 381, 2013.

[18] Mark Lundstrom. Ece 656: Electronic transport in semiconductors (fall 2009), 2009.

Vita

Charles Crawford received a dual Bachelor of Science from Louisiana State University in Shreveport in mathematics and theoretical physics in May 2010. During the fall of 2010 he accepted an internship at the National Aeronautics and Space Administration's Johnson Space Center (NASA-JSC) in Houston. There he performed various tasks in the Applied Aerosciences and Computational Fluid Dynamics Branch (EG3). In his spare time Charles enjoys soccer, playing frisbee with his dog, and playing guitar. With the completion of the requirements at the University of New Orleans, Charles will have a Master of Science in Applied Physics degree.